

# BIOLOGICALLY PLAUSIBLE ONLINE HEBBIAN META-LEARNING: TWO-TIMESCALE LOCAL RULES FOR SPIKING NEURAL BRAIN INTERFACES

**Sriram V.C. Nallani**  
University of Maryland, College Park

**Gautham Ramachandran**  
YCombinator S25

**Sahil Shah**  
University of Maryland, College Park

## ABSTRACT

Brain-Computer Interfaces face challenges from neural signal instability and memory constraints for real-time implantable applications. We introduce an online SNN decoder using local three-factor learning rules with dual-timescale eligibility traces that avoid backpropagation through time while maintaining competitive performance. Our approach combines error-modulated Hebbian updates, fast/slow trace consolidation, and adaptive learning rate control, requiring only  $O(1)$  memory versus  $O(T)$  for BPTT methods. Evaluations on two primate datasets achieve comparable decoding accuracy (Pearson  $R \geq 0.63$  Zenodo,  $R \geq 0.81$  MC Maze) with 28–35% memory reduction and faster convergence than BPTT-trained SNNs. Closed-loop simulations with synthetic neural populations demonstrate adaptation to neural disruptions and learning from scratch without offline calibration. This work enables memory-efficient, continuously adaptive neural decoding suitable for resource-constrained implantable BCI systems.

## 1 INTRODUCTION

Brain-Computer Interfaces (BCIs) translate neural activity into control signals, bypassing conventional neuromuscular pathways (Pandarinath et al., 2017; Shih et al., 2012; Wolpaw et al., 2002). Invasive approaches provide high-fidelity recordings but face barriers including signal instability, noise, and resource constraints, motivating adaptive, efficient, and biologically grounded decoders (Furber et al., 2014; Roy et al., 2019; Taeckens & Shah, 2024; Hussain et al., 2015; Bhaduri et al., 2018). Neural decoding has progressed from classical methods like Kalman filters to deep learning approaches. However, traditional methods struggle with non-stationarities while deep models require frequent recalibration (Wu et al., 2004; Huang et al., 2021) (Shaikh et al., 2019). Our approach builds upon three-factor learning rules and multi-timescale plasticity (detailed background in Appendix F).

### 1.1 CHALLENGES AND MOTIVATION

Challenges remain in BCI development:

- (a) **Signal non-stationarity:** Neural recordings drift due to factors like electrode encapsulation and neural plasticity, requiring frequent recalibration. This necessitates continuous online adaptation to maintain performance without interrupting the user’s experience (Dangi et al., 2014; Ganguly & Carmena, 2009; Wolpaw et al., 2002).
- (b) **High dimensionality and noise:** Electrophysiological data are noisy and high-dimensional, complicating low-latency decoding. SNNs, with their sparse activity and event-driven nature, offer potential advantages in managing these characteristics (Huang et al., 2021; Bhaduri et al., 2018).
- (c) **Cross-session/subject variability:** Models often fail to generalize across sessions or individuals without retraining. An adaptive learning mechanism is necessary to address this.

- (d) **Computational constraints:** Many advanced decoders, reliant on backpropagation through time (BPTT) and large batch updates, are ill-suited for power- and memory-constrained implantable systems. Error backpropagation, a foundation of many deep learning approaches, is also considered biologically implausible in neural circuits due to the weight transport problem, which posits the unlikely existence of symmetric backward connections in the brain (Lillicrap et al., 2020). Combined with on-chip learning constraints in neuromorphic systems (Basu et al., 2022), this motivates BPTT-free local rules.

We evaluate our approach in closed-loop settings because these are necessary for capturing the dynamic co-adaptation between neural activity and decoder learning—an interaction that does not emerge in static, open-loop (offline) analyses (Carmena, 2013; Dangi et al., 2014; Orsborn et al., 2014; Sadtler et al., 2014). Reinforcement learning decoders and meta-learning for automatic plasticity tuning have also been explored. We incorporate meta-learning because it allows the network to ‘learn how to learn,’ enabling rapid adaptation to new tasks or changing neural dynamics by adjusting its own plasticity mechanisms based on experience, a concept supported by research into adaptive systems (Andrychowicz et al., 2016; Finn et al., 2017; Gu et al., 2019; Hochreiter et al., 2001; Miconi et al., 2018; Shervani-Tabar & Rosenbaum, 2023). Spiking Neural Networks (SNNs) equipped with reward-modulated spike-timing-dependent plasticity (R-STDP) enable low-latency, energy-efficient adaptation, further justifying our choice of SNNs as the foundational architecture (Taeckens & Shah, 2024) (see Appendix D for SNN background).

Existing approaches often address these elements separately, lacking a unified mechanism that integrates multi-factor plasticity, two-timescale consolidation, and online meta-learning within an SNN framework. This paper introduces an *online adaptive SNN decoder* that combines these components. Our framework, featuring local Hebbian updates (chosen for their biological relevance and computational locality), fast/slow weight consolidation (to address the stability-plasticity dilemma), and online meta-learning of learning rates (for autonomous adaptation):

- Avoids backpropagation through time, thereby reducing memory and computational overhead in a manner compatible with implantable systems.
- Provides per-sample online adaptation to neural non-stationarities, reducing the need for explicit recalibration and supporting long-term BCI use.
- Is evaluated on two primate intracortical datasets (MC Maze and Zenodo Indy) to benchmark decoding accuracy against state-of-the-art offline decoders before assessing online capabilities.
- Is designed to operate with a minimal memory footprint suitable for real-time, implantable BCI hardware. The learning rule is entirely local, requiring no backprop graphs or replay buffers, only short eligibility traces, aligning with requirements for neuromorphic on-chip learning (Davies et al., 2018; Indiveri & Liu, 2015; Merolla et al., 2014).

## 1.2 RELATED WORK

**Local three-factor SNN learning.** Classical spike-timing-dependent plasticity (STDP) uses pre- and postsynaptic spike timing for unsupervised learning but lacks task-specific supervision (Song et al., 2000; Caporale & Dan, 2008). Three-factor extensions incorporate modulatory signals: reward-modulated STDP uses sparse, delayed dopamine-like signals (Florian, 2007; Frémaux & Gerstner, 2016; Izhikevich, 2007), while eligibility trace methods like SuperSpike and e-prop use broadcast error signals with local traces (Zenke & Ganguli, 2018; Bellec et al., 2020). These approaches enable online learning without time-unrolled graphs but differ in trace derivation and error propagation mechanisms. Hardware demonstrations of local STDP/three-factor rules include floating-gate and dendritic designs (Gopalakrishnan & Basu, 2017; Hussain et al., 2015).

**Surrogate gradient and BPTT SNN training.** Modern SNN training often employs surrogate gradients to handle spike non-differentiability, enabling backpropagation through time with strong supervision (Neftci et al., 2019). While suitable for offline training, BPTT requires  $O(T)$  memory for computational graph storage ( $T$  as in timesteps) and is considered biologically implausible due to weight transport requirements. Recent advances improve gradient flow and temporal alignment but maintain the fundamental BPTT framework.

**Adaptive and online BCI decoders.** Traditional BCI decoders like Kalman filters adapt via parameter updates but struggle with non-stationarities. Deep learning approaches achieve higher performance

but require large amounts of data (Huang et al., 2021). Closed-loop adaptation and co-adaptive systems address decoder-user interaction but often rely on batch updates rather than continuous online learning (Carmena, 2013; Dangi et al., 2014; Orsborn et al., 2014; Bhaduri et al., 2018). From a hardware perspective, neuromorphic implementations favor local, on-chip learning rules (Basu et al., 2022).

**Positioning.** Our approach combines local three-factor learning with dense per-timestep error signals, dual-timescale eligibility traces, and hardware-friendly implementations. Unlike existing methods, we frame eligibility traces as *Hebbian accumulators modulated by reinforcement* rather than BPTT-approximating gradient surrogates, enabling continuous online adaptation with  $O(1)$  memory scaling and biological plausibility.

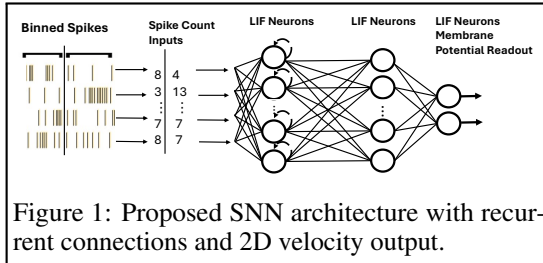
## 2 PROPOSED SNN ARCHITECTURE AND LEARNING ALGORITHM

**Problem Setup and Notation.** We observe spike count vectors  $\mathbf{x}_t \in \mathbb{R}^N$  and predict 2D velocity  $\mathbf{y}_t \in \mathbb{R}^2$  at time bins  $t = 1, \dots, T$ . Hidden layer  $k$  has membrane potentials  $\mathbf{u}_t^{(k)}$ , spikes  $\mathbf{s}_t^{(k)}$ , with the first layer maintaining recurrent state  $\mathbf{s}_{t-1}^{(1)}$ . The final layer’s membrane potentials directly represent velocity predictions:  $\hat{\mathbf{y}}_t = \mathbf{u}_t^{(3)}$ . We train online by minimizing per-timestep squared error  $\mathcal{L}_t = \|\hat{\mathbf{y}}_t - \mathbf{y}_t\|_2^2$  using a local three-factor rule with dual eligibility traces. No unrolled computational graph or replay buffer is required.

Table 1: Key notation and symbols

Symbol	Description
$\mathbf{x}_t$	Input spike count vector at time $t$
$\mathbf{y}_t$	Target 2D velocity at time $t$
$\hat{\mathbf{y}}_t$	Predicted 2D velocity at time $t$
$\mathbf{u}_t^{(k)}$	Membrane potentials for layer $k$ at time $t$
$\mathbf{s}_t^{(k)}$	Spike outputs for layer $k$ at time $t$
$d_{\text{LIF}}$	Surrogate gradient (neuronal sensitivity)
$E^{\text{fast}}, E^{\text{slow}}$	Fast and slow eligibility traces
$\lambda_{\text{fast}}, \lambda_{\text{slow}}$	Decay coefficients: $e^{-\Delta t / \tau_{\text{fast/slow}}}$
$\tau_{\text{fast}}, \tau_{\text{slow}}$	Time constants for eligibility traces (120ms, 700ms)
$\alpha_{\text{mix}}$	Mixing coefficient for combining fast/slow traces
$\eta_{\text{fast}}, \eta_{\text{slow}}$	Fast and slow learning rates
$K$	Consolidation window (timesteps)
$\mathcal{R}(\cdot)$	RMS normalization function

### 2.1 CORE ARCHITECTURE



Our network is built around Leaky Integrate-and-Fire (LIF) neurons, chosen for their balance of biological realism and computational tractability (see Appendix D for background). Each neuron’s membrane potential  $u_i(t)$  integrates incoming synaptic currents, leaks with a decay factor  $\beta$ , and emits a spike when reaching a threshold (normalized to 1). Post-spiking, the membrane potential

resets according to:

$$u_i(t+1) = \beta u_i(t) + I_i(t) - s_i(t).$$

Learning uses surrogate gradient methods (Neftci et al., 2019; Zenke & Vogels, 2021; Bellec et al., 2020) to handle spike non-differentiability, creating a neuronal sensitivity gate that focuses plasticity on neurons near threshold. Full derivations and homeostatic controls are in Appendix B. We use  $d_{\text{LIF}}$  as a per-timestep local gate, without temporal backpropagation (Algorithm 6).

The three-layer architecture (Figure 1) includes recurrent connections in the first hidden layer. Unlike baseline models that use spike rates, our SNN processes raw spike counts directly. Full details are in Appendix A.

## 2.2 LEARNING ALGORITHM

Our online learning rule operates through a unified mechanism where local Hebbian updates are accumulated in dual-timescale eligibility traces, then applied through fast and slow weight update pathways. This design addresses the core challenge of online adaptation: maintaining rapid responsiveness to immediate errors while preserving stable long-term learning.

**Notation.** For layer  $\ell$ , let  $W^{(\ell)} \in \mathbb{R}^{n_{\text{post}} \times n_{\text{pre}}}$  be the weight matrix,  $\text{pre}_t^{(\ell)} \in \mathbb{R}^{n_{\text{pre}}}$  the presynaptic activity at time  $t$ ,  $\mathbf{e}_t^{(\ell)} \in \mathbb{R}^{n_{\text{post}}}$  a layer-local error drive, and  $d_t^{(\ell)} \in \mathbb{R}^{n_{\text{post}}}$  the postsynaptic sensitivity (LIF surrogate gradient; large near threshold). All vectors are column vectors;  $\odot$  denotes elementwise product; outer products are written  $a b^\top$ . We set  $\text{pre}_t^{(1)} = \mathbf{x}_t$ ,  $\text{pre}_t^{(2)} = \mathbf{s}_t^{(1)}$ ,  $\text{pre}_t^{(3)} = \mathbf{s}_t^{(2)}$ , and for the recurrent path use  $\text{pre}_t^{(\text{rec})} = \mathbf{s}_{t-1}^{(1)}$ .

**Three-Factor Hebbian Plasticity and Eligibility Traces.** *Layer-local error drives (spatial-only using current feedforward weights):*

$$\tilde{\mathbf{e}}_t^{(3)} := \mathcal{R}(\mathbf{y}_t - \hat{\mathbf{y}}_t), \quad \mathbf{e}_t^{(2)} := (W^{(3)})^\top \tilde{\mathbf{e}}_t^{(3)}, \quad \mathbf{e}_t^{(1)} := (W^{(2)})^\top \mathbf{e}_t^{(2)}.$$

The algorithm begins with local three-factor Hebbian updates that capture coincident presynaptic activity, postsynaptic sensitivity, and error signals:

$$\Delta W_{\text{hebb}}^{(\ell)}(t) = (\tilde{\mathbf{e}}_t^{(\ell)} \odot d_t^{(\ell)}) (\text{pre}_t^{(\ell)})^\top. \quad (1)$$

The same rule updates  $W^{(\text{rec})}$  with  $\text{pre}_t^{(\text{rec})}$ . Rather than applying these updates directly, each synapse accumulates them in dual eligibility traces with different decay timescales:

$$E_{\text{fast}}^{(\ell)}(t) = \lambda_{\text{fast}} E_{\text{fast}}^{(\ell)}(t-1) + \Delta W_{\text{hebb}}^{(\ell)}(t), \quad (2)$$

$$E_{\text{slow}}^{(\ell)}(t) = \lambda_{\text{slow}} E_{\text{slow}}^{(\ell)}(t-1) + \Delta W_{\text{hebb}}^{(\ell)}(t), \quad (3)$$

where  $\lambda_{\text{fast}} = \exp(-\Delta t / \tau_{\text{fast}})$  and  $\lambda_{\text{slow}} = \exp(-\Delta t / \tau_{\text{slow}})$ . These are combined as:

$$E_{\text{comb}}^{(\ell)}(t) = \alpha_{\text{mix}} E_{\text{fast}}^{(\ell)}(t) + (1 - \alpha_{\text{mix}}) E_{\text{slow}}^{(\ell)}(t). \quad (4)$$

**Dual-Timescale Weight Updates.** The eligibility traces drive two parallel update streams that address different temporal requirements (Pfister & Gerstner, 2006; Benna & Fusi, 2016). Fast updates apply the combined trace immediately:

$$W^{(\ell)} \leftarrow W^{(\ell)} + \eta_{\text{fast}} E_{\text{comb}}^{(\ell)}(t),$$

providing rapid adaptation. Simultaneously, a momentum-smoothed accumulator builds evidence for stable changes:

$$G^{(\ell)}(t) = \mu G^{(\ell)}(t-1) + (1 - \mu) E_{\text{comb}}^{(\ell)}(t).$$

Every  $K$  timesteps, this drives slow updates:

$$W^{(\ell)} \leftarrow W^{(\ell)} + \eta_{\text{slow}} \mathcal{R}(\bar{G}_K^{(\ell)}(t)),$$

where  $\mathcal{R}(\cdot)$  provides RMS normalization and  $\bar{G}_K^{(\ell)}(t)$  is the  $K$ -step average. This dual pathway balances plasticity with stability.

**Stability and Meta-Learning.** Three mechanisms prevent instability during continuous adaptation. First, RMS normalization maintains bounded signal magnitudes using exponential moving averages (Bhaduri et al., 2018):

$$\begin{aligned} \text{RMS}_{\text{err}}^2(t) &= \lambda_{\text{rms}} \text{RMS}_{\text{err}}^2(t-1) + (1 - \lambda_{\text{rms}}) \|\mathbf{e}_t^{(\ell)}\|^2, \\ \tilde{\mathbf{e}}_t^{(\ell)} &= \mathbf{e}_t^{(\ell)} / \sqrt{\text{RMS}_{\text{err}}^2(t) + \epsilon}, \quad \tilde{\mathbf{s}}_t^{(\ell)} = \mathbf{s}_t^{(\ell)} / \sqrt{\text{RMS}_{\text{spk}}^2(t) + \epsilon}. \end{aligned}$$

Second, per-neuron weight projection prevents runaway growth:

$$W_{i:}^{(\ell)} \leftarrow \min\left(1, \frac{c_\ell}{\|W_{i:}^{(\ell)}\|_2 + \epsilon}\right) W_{i:}^{(\ell)}, \quad c_\ell = 6.$$

Third, an adaptive controller adjusts learning rate multipliers based on windowed performance. At boundaries (every  $K$  timesteps), the window-averaged loss drives multiplicative updates:

$$\begin{aligned} \bar{\mathcal{L}}_t &= \frac{1}{K} \sum_{s=t-K+1}^t \mathcal{L}_s, \quad z_t = \text{sign}(\bar{\mathcal{L}}_{t-1} - \bar{\mathcal{L}}_t), \\ p_{t+1} &= \text{clip}(p_t[1 + \eta_{\text{meta}} z_t]; p_{\min}, p_{\max}), \quad s_{t+1} = \text{clip}(s_t[1 + \eta_{\text{meta}} z_t]; s_{\min}, s_{\max}), \end{aligned}$$

where effective learning rates become  $\eta_{\text{fast}}^{(t+1)} = p_{t+1} \eta_{\text{fast}}^{(0)}$  and  $\eta_{\text{slow}}^{(t+1)} = s_{t+1} \eta_{\text{slow}}^{(0)}$ . When loss decreases, multipliers increase plasticity; when loss stagnates, they shrink for stability. In practice, we also apply a lightweight error-modulated lookup table (LUT) that discretizes per-timestep output errors into 16 buckets and rescales the fast learning rate accordingly. This hardware-friendly heuristic serves as a coarse neuromodulatory signal that modulates plasticity without introducing additional complexity (see Appendix B.3 for details).

### Complexity and Memory Analysis.

Table 2: Memory usage (MB) for SNN architectures (120-timestep sequences)

Component	96-256-128-2		96-1024-512-2	
	Online	BPTT	Online	BPTT
Static (MB)	1.41	1.88	19.15	25.54
Dynamic (MB)	—	0.29	—	1.13
<b>Total peak(MB)</b>	<b>1.41</b>	<b>2.17</b>	<b>19.15</b>	<b>26.67</b>

**Time and memory.** Per timestep, the update requires current activations, integer RMS statistics, and two eligibility matrices per trained weight. Memory complexity is  $O(P)$  in parameters and  $O(1)$  in sequence length  $T$ ; BPTT requires additional  $O(T)$  activations. Training memory is  $O(1)$  in sequence length  $T$  (parameters + traces + statistics), whereas BPTT requires  $O(T)$  activations for gradient computation.

**Measured peak memory (MB)** at 120 timestep sequences: 96-256-128-2 architecture shows Online 1.41 vs BPTT 2.17 (35% reduction); 96-1024-512-2 shows Online 19.15 vs BPTT 26.67 (28% reduction) as per Table 2. These results match the analytic  $O(1)/O(T)$  behavior and become more pronounced for longer sequences (Figure 8). Reasoning and implementation details are in Appendix E.

## 3 EXPERIMENTAL METHODS

**Datasets.** We evaluate on two public intracortical datasets: *MC Maze* (Churchland & Kaufman, 2022) (10 ms resampling, 80 ms kinematic lag) and *Zenodo Indy* (O’Doherty et al., 2017) (50 ms bins, zero lag). Targets are 2D velocities derived from positions. Our SNNs consume raw spike counts; KF/LSTM baselines consume rate-normalized inputs. Splits avoid leakage (MC Maze by trials; Zenodo chronologically).

**Baselines.** Kalman Filter (online sequential decoder (Li et al., 2011; Sussillo et al., 2016)), LSTM (Premchand et al., 2020), BPTT-SNN, and the proposed Online SNN. BPTT-SNN and Online SNN

have identical architectures. We evaluate the Online SNN in *batched* and *timestep-wise* modes. All SNN variants use raw counts; baselines use normalized firing rates. Implementations use PyTorch/snnTorch. Baseline hyperparameters in Table 4.

**Metrics.** We use Pearson correlation coefficient ( $R$ ) between predicted and true velocity components:  $R = \frac{\sum_t (\hat{v}_t - \bar{\hat{v}})(v_t - \bar{v})}{\sqrt{\sum_t (\hat{v}_t - \bar{\hat{v}})^2} \sqrt{\sum_t (v_t - \bar{v})^2}}$ . Results are mean  $\pm$  SEM across data splits. For closed-loop tasks, we measure time-to-target. Statistical significance uses Welch’s t-test ( $n = 10$  runs). Significance: \*  $p < 0.05$ , \*\*  $p < 0.01$ , \*\*\*  $p < 0.001$ . Full details are in Appendix A.

## 4 RESULTS

### Comparative Decoder Performance on Offline Datasets.

We benchmarked the Online SNN (in its Batched Online mode for these offline tests) against a Kalman Filter (KF), a Long Short-Term Memory network (LSTM), and an offline-trained Spiking Neural Network using Backpropagation Through Time (BPTT-SNN). For the MC Maze dataset, the SNN architecture consisted of 182 input neurons (91 from M1 and 91 from PMd cortices). The MC Maze network followed a 182-1024-512-2 architecture. For the Zenodo Indy dataset, the architecture used 96 input neurons (from M1 cortex). Zenodo Indy network followed a 96-256-128-2 architecture. These architectures were kept consistent between the Online SNN and BPTT-SNN for fair comparison. Performance, measured by Pearson correlation ( $R$ ) for X and Y velocity predictions, is shown in Figures 2a (MC Maze) and 2b (Zenodo Indy). The results highlight dataset-dependent strengths but demonstrate statistically meaningful decoding capabilities for most models on both datasets.

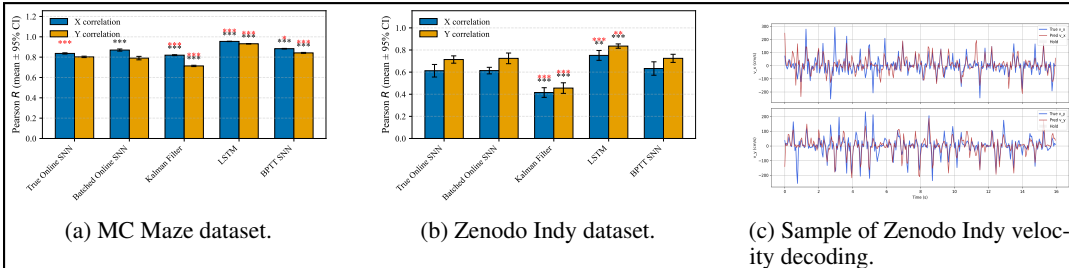


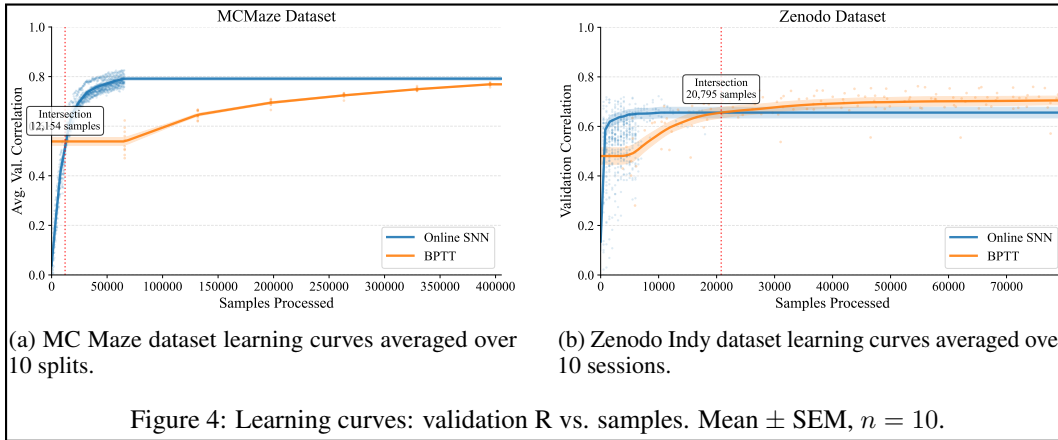
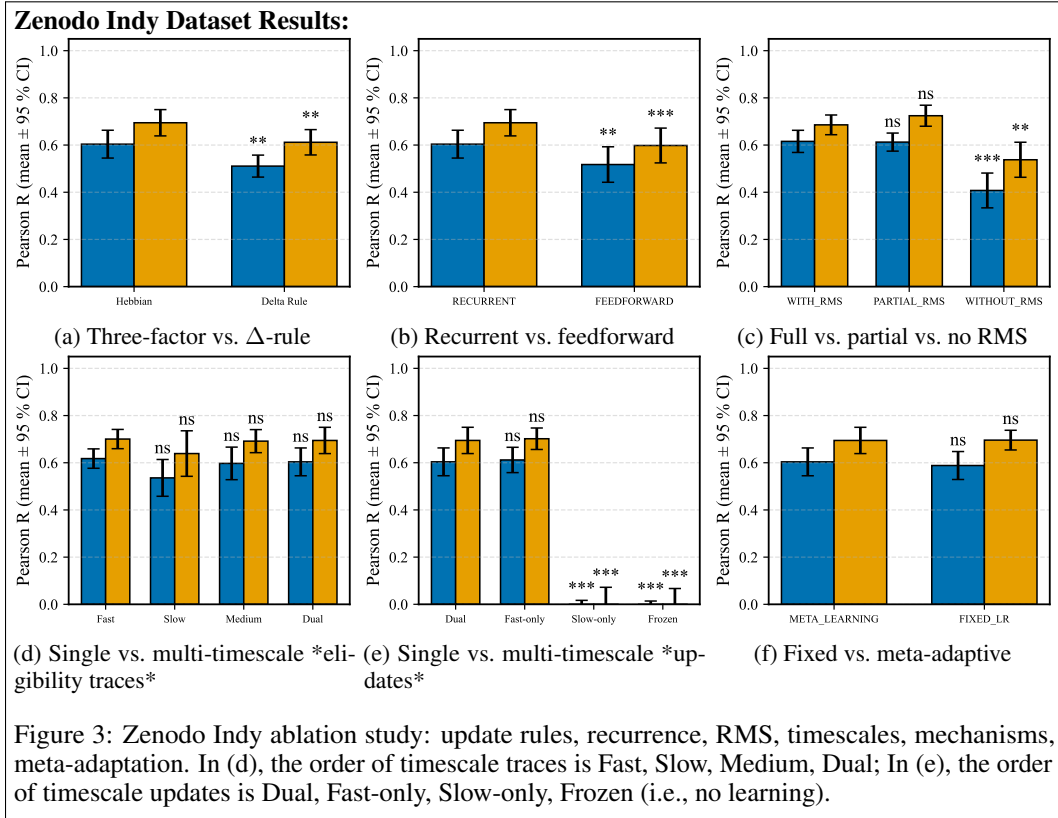
Figure 2: Decoder performance: Pearson R, mean  $\pm$  SEM,  $n = 10$ . **Order of Decoders in (a) and (b): True Online SNN, Batched Online SNN, Kalman Filter, LSTM, BPTT SNN.** MC Maze decoder comparison shown in (a), Zenodo Indy decoder comparison shown in (b). Performance of True (Timestep-wise) Online SNN on Zenodo Indy session 20161013\_03 shown in (c). In figures (a) and (b), red significance stars indicate comparison with the Batched Online SNN; black significance stars indicate comparison with True (Timestep-wise) Online SNN.

### Ablation Studies

Our ablation studies reveal dataset-dependent component contributions (methodology in Appendix G; further analysis in Appendix C). The Three-factor vs. delta rule comparison shows that neuronal sensitivity gating ( $d_{LIF}$ ) is important for Zenodo Indy but negligible for MC Maze, due to differences in temporal alignment and noise characteristics. Here, the delta rule refers to a simplified update that removes the LIF surrogate gradient term, reducing to  $\Delta W = e_t(\text{pre}_t)^\top$  without neuronal sensitivity modulation. MC Maze’s 80ms kinematic lag and trial structure provide higher effective signal-to-noise ratios, making simple delta updates sufficient. Zenodo Indy’s continuous, self-paced reaches with mixed sorting quality benefit from the three-factor gate’s noise robustness and temporal precision (Figure 3).

### Cross-Dataset Analysis and Interpretation:

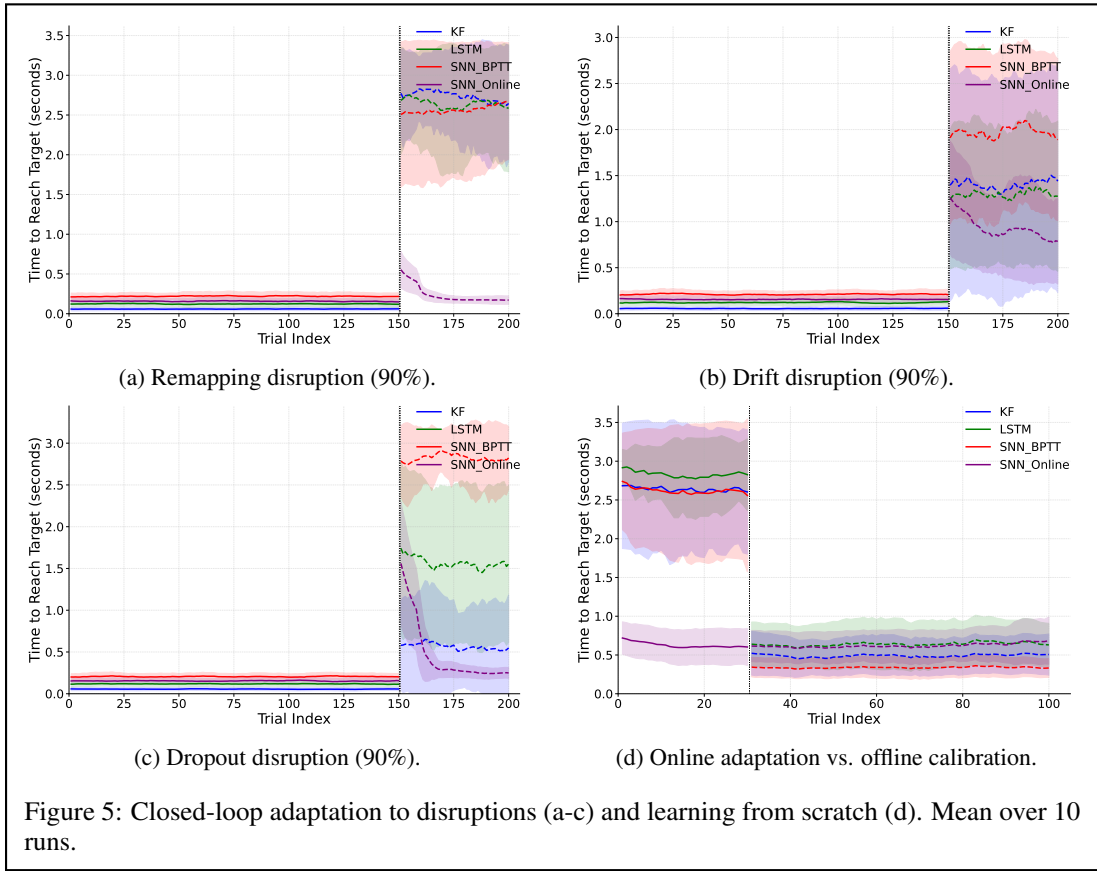
The trends are both universal and dataset-specific (MC Maze results in Appendix C). The **learning rule** is task dependent: the three-factor mechanism is important on Zenodo but not on MC Maze. The **architecture** benefits from recurrence on both datasets—strongly on Zenodo and moderately on MC Maze. For the **update mechanism**, using both fast and slow updates is the safest choice; slow-only



and frozen are harmful everywhere. Fast-only can be competitive on Zenodo but is slightly worse than dual on MC Maze. The optimal **trace timescale** differs by dataset: slow or dual on MC Maze, fast on Zenodo. **RMS normalization** is important across datasets and necessary on Zenodo; partial RMS should generally be avoided due to axis trade-offs. **Meta-adaptation** yields small gains at best; keep it when resources allow, but it is not the primary driver of performance.

#### 4.1 ONLINE SNN LEARNING DYNAMICS: EFFICIENCY AND ADAPTATION

A comparison of the Online SNN (trained for 5 epochs, with an effective batch size of 1 due to sample-wise updates, hence a low number of epochs) with the BPTT-SNN (trained for 50 epochs, batch size 128) on the MC Maze dataset reveals a key advantage of the online learning approach (Figure 4). The Online SNN demonstrates faster convergence to a high level of performance. Despite starting from almost zero correlation, the Online SNN rapidly improves, surpassing the BPTT-SNN



initially within the first 3 epochs itself. However, due to the sophisticated Adam optimizer, the BPTT SNN attains a higher Pearson correlation as training progresses over more epochs (50). MCMaze had around 65000 samples in 1 epoch; Zenodo had around 10000. This rapid, sample-wise adaptation capability indicates that the Online SNN can achieve proficient decoding with less exposure to the training dataset, highlighting greater learning efficiency.

#### 4.2 CLOSED-LOOP SIMULATIONS WITH SYNTHETIC NEURAL POPULATIONS

**Disruption Ablations (Remapping, Drift, Dropout)** Decoder resilience to neural nonstationarities was assessed via three simulated disruptions representing realistic BCI challenges: 90% neural remapping (simulating electrode shift or tissue encapsulation changing preferred directions), 90% firing rate drift (simulating signal degradation reducing maximum rates by 45% and increasing baseline rates by 90%), and 90% neuron dropout (simulating electrode failure or tissue death silencing 90% of recording sites) (Figures 5a, 5b, 5c). Closed-loop hyperparameters in Appendix H.0.5.

**Phase 1 (Pre-Disruption Performance):** Initially (trials 0-150), all four decoders (Kalman Filter - KF, LSTM, BPTT SNN, Online SNN) exhibited proficient and stable control. As seen across Figures 5a, 5b, and 5c, mean time-to-target was consistently low, reflecting baseline performance.

**Phase 2 (Post-Disruption Adaptation):** Following disruption at trial 150 (vertical dotted line), performance trajectories diverged:

**Online SNN (Purple Dashed Line):** Displayed robustness and rapid adaptation. Under 90% **Remapping** (Figure 5a), after a minor transient performance dip (starting at 0.5 s), it rapidly readapted to pre-disruption levels with sustained consistency ( $\leq 0.30s$ ) in  $\sim 20$  reaches. With 90% **Dropout** (Figure 5c), its performance dropped (1.5 s to reach target) but readapted to the pre-disruption levels, also in  $\sim 15-20$  reaches. Similarly, under 90% **Drift** (Figure 5b), the Online

SNN adapted in 20 reaches as the time to reach target decreased from 1.5 s to about 0.75. Online SNN’s ongoing parametric adjustments mitigated these nonstationarities.

**Fixed-Parameter Decoders (KF - Blue; LSTM - Green; BPTT SNN - Red):** These decoders with fixed parameters demonstrated vulnerability. LSTM and BPTT SNN performance declined due to all disruptions, consistently taking over 1.5 s to reach target, compared to their quick  $< 0.30$  s time before disruption. The KF performance declined less due to dropout disruption as compared to a greater performance reduction on other two disruptions.

These results demonstrate the Online SNN’s advantage in maintaining performance via continuous adaptation when facing diverse neural nonstationarities, an important feature for practical BCIs.

**Online Adaptation vs. Offline Calibration (No-Pretrain Comparison)** This experiment (Figure 5d) compared the Online SNN’s ability to learn from scratch against offline-trained decoders requiring separate calibration.

**Phase 1 (Online Data Collection / Initial Adaptation;  $\sim 30$  reaches):** During initial interaction: **Online SNN (Purple Solid Line):** Beginning with random weights and no pretraining, the online SNN initially required 0.75 seconds to reach the target. Through continuous learning during task execution, performance steadily improved to 0.6 seconds and maintained this level consistently. Note that since no decoder received pretraining, the online SNN’s initial performance of 0.75 seconds represents an improvement over the typical 0.25–0.3 second baselines achievable with pretrained systems.

**Fixed-Weight Decoders (KF, LSTM, BPTT SNN):** These approaches operated with static, randomly initialized weights throughout testing. Without the ability to adapt, they exhibited highly variable performance with frequent failures to complete the task within the 3-second timeout limit.

**Phase 2 (Post-Calibration Evaluation;  $\sim 70$  reaches):** After data collection and batch calibration: **Offline-Trained Decoders:** After calibration on their own collected interaction data, all decoders achieved performance comparable to Online SNN. **Online SNN:** Having adapted in Phase 1, it maintained stable performance.

Figure 5d demonstrates the Online SNN’s capacity for learning from scratch. It achieved proficient control through direct interaction without requiring separate offline calibration. While offline-trained decoders performed well after calibration, they were ineffective during initial data gathering. The Online SNN enables immediate BCI utility and continuous adaptation from the first interaction.

## 5 DISCUSSION

Our three-factor rule differs from classic reward-modulated STDP in that it uses a dense kinematic error for frame-wise credit assignment while remaining local at the synapse. Surrogate gradients provide a sensitivity gate that confines plasticity to neurons near threshold, avoiding the weight-transport and memory costs of BPTT (Seung, 2003; Izhikevich, 2007; Frémaux & Gerstner, 2016; Neftci et al., 2019; Bellec et al., 2020; Zenke & Vogels, 2021).

Integrating fast/slow consolidation directly into the online updater resolves a stability–plasticity tension without replay or mini-batches. Fast traces enable rapid correction; slow consolidation preserves durable structure, echoing early/late LTP accounts and synaptic memory theories (Fusi et al., 2005; Benna & Fusi, 2016; Zenke et al., 2017; Kirkpatrick et al., 2017). This yields  $O(1)$  memory in sequence length and continuous adaptation.

Practically, closed-loop simulations show the updater maintains control under remapping, drift, and dropout, and can learn from scratch, suggesting usefulness for long-running BCIs in non-stationary conditions. Hardware-friendly homeostasis (RMS gating, row-wise renorm) keeps signals bounded, aligning with event-driven deployment targets. A lightweight reward-modulated LUT further adjusts fast plasticity (fast learning rate) using discretized error buckets. Detailed mechanisms are in App. B.

## 6 CONCLUSION

We present a BPTT-free online SNN decoder that combines local three-factor plasticity with dual-timescale consolidation and adaptive learning rate control, achieving competitive decoding with  $O(1)$

memory. The approach adapts continuously to non-stationarities and is compatible with resource-constrained, neuromorphic implementations (Gopalakrishnan & Basu, 2017; Basu et al., 2022; Hasler & Basu, 2025).

**Limitations.** (1) Closed-loop results use synthetic populations; validation on chronic human recordings is still required (Cunningham et al., 2011). (2) The consolidation window  $K$  and reset thresholds are hand-tuned; fully automatic scheduling would improve robustness across tasks. (3) Empirical scaling on neuromorphic devices remains to be demonstrated, despite favorable memory analysis.

## 7 REPRODUCIBILITY

Complete offline hyperparameters in Appendix H.0.4. Epochs for ablations maximum 15. **Evaluation:** 10 independent runs per condition, Welch’s t-tests for significance. **Compute:** PyTorch/snnTorch implementations on single A100/H100 GPU based on availability (part of university HPC Cluster). Closed-loop hyperparameters in Appendix H.0.5. LLM usage disclosure in Appendix 7.

## REFERENCES

- L. F. Abbott and S. B. Nelson. Synaptic plasticity: Taming the beast. *Nature Neuroscience*, 3(11S): 1178–1183, 2000. doi: 10.1038/81453.
- Marcin Andrychowicz, Misha Denil, Sergio Gomez, Matthew Hoffman, David Pfau, Tom Schaul, Brendan Shillingford, and Nando de Freitas. Learning to learn by gradient descent by gradient descent. In *Advances in Neural Information Processing Systems 29 (NeurIPS 2016)*, pp. 3981–3989, 2016.
- Arindam Basu, Charlotte Frenkel, Lei Deng, and Xueyong Zhang. Spiking neural network integrated circuits: A review of trends and future directions. *arXiv preprint*, 2022. Authors listed alphabetically.
- Guillaume Bellec, Franz Scherr, Darjan Salaj, et al. A solution to the learning dilemma for recurrent networks of spiking neurons. *Nature Communications*, 11:3625, 2020. doi: 10.1038/s41467-020-17236-y.
- Marcus K. Benna and Stefano Fusi. Computational principles of synaptic memory consolidation. *Nature Neuroscience*, 19(12):1697–1706, 2016.
- Abhishek Bhaduri, Amitava Banerjee, Subhrajit Roy, Shantanu Kar, and Arindam Basu. Spiking neural classifier with lumped dendritic nonlinearity and binary synapses: A current mode vlsi implementation and analysis. *Neural Computation*, 30(3):723–760, 2018. doi: 10.1162/neco\_a\_01045.
- Guo-qiang Bi and Mu-ming Poo. Synaptic modifications in cultured hippocampal neurons: Dependence on spike timing, synaptic strength, and postsynaptic cell type. *Journal of Neuroscience*, 18(24):10464–10472, 1998.
- Natalia Caporale and Yang Dan. Spike timing-dependent plasticity: A hebbian learning rule. *Annual Review of Neuroscience*, 31:25–46, 2008.
- Jose M. Carmena. Advances in neuroprosthetic learning and control. *PLoS Biology*, 11(5):e1001561, 2013.
- Mark Churchland and Matthew Kaufman. Mc\_maze: macaque primary motor and dorsal premotor cortex spiking activity during delayed reaching (version 0.220113.0400) [data set], 2022. URL <https://doi.org/10.48324/dandi.000128/0.220113.0400>.
- John P. Cunningham, Paul Nuyujukian, Vikash Gilja, Cindy A. Chestek, Stephen I. Ryu, and Krishna V. Shenoy. A closed-loop human simulator for investigating the role of feedback control in brain–machine interfaces. *Journal of Neurophysiology*, 105(4):1932–1949, 2011. doi: 10.1152/jn.00503.2010.

- Siddharth Dangi, Suma Gowda, Hamilton G. Moorman, Amy L. Orsborn, Kelvin So, Maryam Shanechi, and Jose M. Carmena. Continuous closed-loop decoder adaptation with a recursive maximum likelihood algorithm allows for rapid performance acquisition in brain–machine interfaces. *Neural Computation*, 26(9):1811–1839, 2014.
- Mike Davies, Narayan Srinivasa, Tien-Hsin Lin, et al. Loihi: A neuromorphic manycore processor with on-chip learning. *IEEE Micro*, 38(1):82–99, 2018.
- Chelsea Finn, Pieter Abbeel, and Sergey Levine. Model-agnostic meta-learning for fast adaptation of deep networks. In *Proceedings of the 34th International Conference on Machine Learning (ICML 2017)*, volume 70 of *Proceedings of Machine Learning Research*, pp. 1126–1135, 2017.
- R zvan V. Florian. Reinforcement learning through modulation of spike-timing-dependent synaptic plasticity. *Neural Computation*, 19(6):1468–1502, 2007. doi: 10.1162/neco.2007.19.6.1468.
- Nicolas Frémaux and Wulfram Gerstner. Neuromodulated spike-timing-dependent plasticity, and theory of three-factor learning rules. *Frontiers in Neural Circuits*, 9:85, 2016. doi: 10.3389/fncir.2015.00085.
- Steve B. Furber, Francesco Galluppi, Steve Temple, and Luis A. Plana. The spinnaker project. *Proceedings of the IEEE*, 102(5):652–665, 2014.
- Stefano Fusi, Patrick J. Drew, and L. F. Abbott. Cascade models of synaptic plasticity: Toward the goal of understanding cerebral cortex. *Neuron*, 45(4):599–611, 2005.
- Karunesh Ganguly and Jose M. Carmena. Emergence of a stable cortical map for neuroprosthetic control. *PLoS Biology*, 7(7):e1000153, 2009.
- Roshan Gopalakrishnan and Arindam Basu. Triplet spike time-dependent plasticity in a floating-gate synapse. *IEEE Transactions on Neural Networks and Learning Systems*, 28(4):778–790, 2017. doi: 10.1109/TNNLS.2015.2506740.
- Keren Gu, Sam Greydanus, Luke Metz, Niru Maheswaranathan, and Jascha Sohl-Dickstein. Meta-learning biologically plausible semi-supervised update rules. *bioRxiv*, pp. 2019.12.30.891184, 2019. doi: 10.1101/2019.12.30.891184.
- Jennifer Hasler and Arindam Basu. Historical perspective and opportunity for computing in memory using floating-gate and resistive non-volatile computing including neuromorphic computing. *Neuromorphic Computing and Engineering*, 5:12001, 2025. doi: 10.1088/2634-4386/ad9b4a.
- Ahmed Hasssan, Jian Meng, Anupreetham Anupreetham, and Jae-sun Seo. SpQuant-SNN: Ultra-low precision membrane potential with sparse activations unlock the potential of on-device spiking neural networks applications. *Frontiers in Neuroscience*, 18:1440000, 2024. doi: 10.3389/fnins.2024.1440000.
- Donald O. Hebb. *The Organization of Behavior*. Wiley, New York, 1949.
- Sepp Hochreiter, A. Steven Younger, and Peter R. Conwell. Learning to learn using gradient descent. In *Proceedings of the International Conference on Artificial Neural Networks (ICANN 2001)*, pp. 87–94, 2001.
- X. Huang, Y. Xu, J. Hua, W. Yi, H. Yin, R. Hu, and S. Wang. A review on signal processing approaches to reduce calibration time in eeg-based brain–computer interface. *Frontiers in Neuroscience*, 15: 733546, 2021. doi: 10.3389/fnins.2021.733546.
- Shaista Hussain, Shih-Chii Liu, and Arindam Basu. Hardware-amenable structural learning for spike-based pattern classification using a simple model of active dendrites. *Neural Computation*, 27(4):845–897, 2015. doi: 10.1162/NECO\_a\_00713.
- Giacomo Indiveri and Shih-Chii Liu. Memory and information processing in neuromorphic systems. *Proceedings of the IEEE*, 103(8):1379–1397, 2015.
- Eugene M. Izhikevich. Solving the distal reward problem through linkage of STDP and dopamine signaling. *Cerebral Cortex*, 17(10):2443–2452, 2007.

- Diederik P. Kingma and Jimmy Ba. Adam: A method for stochastic optimization. *arXiv preprint*, 2015.
- James Kirkpatrick, Razvan Pascanu, Neil Rabinowitz, et al. Overcoming catastrophic forgetting in neural networks. *Proceedings of the National Academy of Sciences USA*, 114(13):3521–3526, 2017. doi: 10.1073/pnas.1611835114.
- Lukasz Kusmierz, Takuya Isomura, and Taro Toyozumi. Learning with three factors: modulating hebbian plasticity with errors. *Current Opinion in Neurobiology*, 46:170–177, 2017. doi: 10.1016/j.conb.2017.08.020.
- Zhe Li, Joseph E. O’Doherty, Mikhail A. Lebedev, and Miguel A. L. Nicolelis. Adaptive decoding for brain–machine interfaces through bayesian parameter updates. *Neural Computation*, 23(12): 3162–3204, 2011. doi: 10.1162/NECO\_a\_00207.
- Timothy P. Lillicrap, Adam Santoro, Luke Marris, Colin J. Akerman, and Geoffrey Hinton. Backpropagation and the brain. *Nature Reviews Neuroscience*, 21(6):335–346, 2020. doi: 10.1038/s41583-020-0275-8.
- Henry Markram, Joachim L’ubke, Michael Frotscher, and Bert Sakmann. Regulation of synaptic efficacy by coincidence of postsynaptic APs and EPSPs. *Science*, 275(5297):213–215, 1997.
- Szymon Mazurek, E. Paxon Frady, and Friedrich T. Sommer. Three-factor learning in spiking neural networks: An overview of methods and trends from a machine learning perspective. *arXiv preprint*, 2025.
- Paul A. Merolla, John V. Arthur, Rodrigo Alvarez-Icaza, et al. A million spiking-neuron integrated circuit with a scalable communication network and interface. *Science*, 345(6197):668–673, 2014.
- Thomas Miconi, Jeff Clune, and Kenneth O. Stanley. Differentiable plasticity: Training plastic neural networks with backpropagation. In *Proceedings of the 35th International Conference on Machine Learning (ICML 2018)*, volume 80 of *Proceedings of Machine Learning Research*, pp. 3559–3568, 2018.
- Milad Mozafari et al. First-spike based visual categorization using reward-modulated STDP. *arXiv preprint*, 2018.
- Emre O. Neftci, Hesham Mostafa, and Friedemann Zenke. Surrogate gradient learning in spiking neural networks: Bringing the power of gradient-based optimization to spiking neural networks. *IEEE Signal Processing Magazine*, 36(6):51–63, 2019. doi: 10.1109/MSP.2019.2931595.
- Joseph E. O’Doherty, Mariana M. B. Cardoso, Joseph G. Makin, and Philip N. Sabes. Nonhuman primate reaching with multichannel sensorimotor cortex electrophysiology. Dataset, 2017. URL <https://doi.org/10.5281/zenodo.583331>.
- Amy L. Orsborn, Hamilton G. Moorman, Simon A. Overduin, et al. Closed-loop decoder adaptation shapes neural plasticity for skillful neuroprosthetic control. *Neuron*, 82(6):1380–1393, 2014.
- Chethan Pandarinath et al. High performance communication by people with paralysis using an intracortical brain–computer interface. *eLife*, 6:e18554, 2017. doi: 10.7554/eLife.18554.
- Jean-Pascal Pfister and Wulfram Gerstner. Triplets of spikes in a model of spike timing-dependent plasticity. *Journal of Neuroscience*, 26(38):9673–9682, 2006.
- Brian Premchand, Kyaw Kyar Toe, Chuanchu Wang, Shoeb Shaikh, Camilo Libedinsky, Kai Keng Ang, and Rosa Q. So. Decoding movement direction from cortical microelectrode recordings using an lstm-based neural network. In *Proceedings of the 42nd Annual International Conference of the IEEE Engineering in Medicine & Biology Society (EMBC)*, pp. 3007–3010, Montreal, QC, Canada, 2020. IEEE. doi: 10.1109/EMBC44109.2020.9175593.
- Kaushik Roy, Akhilesh Jaiswal, and Priyadarshini Panda. Towards spike-based machine intelligence with neuromorphic computing. *Nature*, 575(7784):607–617, 2019. doi: 10.1038/s41586-019-1677-2.

- Patrick T. Sadtler, Kevin M. Quick, Matthew D. Golub, et al. Neural constraints on learning. *Nature*, 512(7515):423–426, 2014.
- Samuel Schmidgall, Joe Hays, and Alexander Ororbia. Meta-spikepropamine: learning to learn with synaptic plasticity in spiking neural networks. *Frontiers in Neuroscience*, 17:1183321, 2023. doi: 10.3389/fnins.2023.1183321.
- H. Sebastian Seung. Learning in spiking neural networks by reinforcement of stochastic synaptic transmission. *Neural Computation*, 15(8):1821–1849, 2003.
- Shoeb Shaikh, Na Duong Tran, G. Sunil Krishna, Jyotibdha Acharya, Arindam Basu, Kian Hsiang Chua, Nitish V. Thakor, and Haizhou Li. Neuromorphic decoders that outperform kalman filter and neural networks. *IEEE Transactions on Biomedical Circuits and Systems*, 13(6):1615–1624, 2019. doi: 10.1109/TBCAS.2019.2944486.
- Navid Shervani-Tabar and Robert Rosenbaum. Meta-learning biologically plausible plasticity rules with random feedback pathways. *Nature Communications*, 14:1555, 2023. doi: 10.1038/s41467-023-37562-1.
- Jerry J. Shih, Dean J. Krusienski, and Jonathan R. Wolpaw. Brain–computer interfaces in medicine. *Mayo Clinic Proceedings*, 87(Suppl 1):S107–S110, 2012.
- S. Song, K. D. Miller, and L. F. Abbott. Competitive hebbian learning through spike-timing-dependent synaptic plasticity. *Nature Neuroscience*, 3(9):919–926, 2000.
- David Sussillo, Sergey D. Stavisky, Jonathan C. Kao, Stephen I. Ryu, and Krishna V. Shenoy. Making brain–machine interfaces robust to future neural variability. *Nature Communications*, 7:13749, 2016. doi: 10.1038/ncomms13749.
- Elijah A. Taeckens and Sahil Shah. A spiking neural network with continuous local learning for robust online brain–machine interface. *Journal of Neural Engineering*, 20(6):066042, 2024. doi: 10.1088/1741-2552/ad1787.
- Gina G. Turrigiano and Sacha B. Nelson. Homeostatic plasticity in the developing nervous system. *Nature Reviews Neuroscience*, 5(2):97–107, 2004. doi: 10.1038/nrn1328.
- Jonathan R. Wolpaw, Niels Birbaumer, Dennis J. McFarland, Gert Pfurtscheller, and Theresa M. Vaughan. Brain–computer interfaces for communication and control. *Clinical Neurophysiology*, 113(6):767–791, 2002.
- Wei Wu, Michael J. Black, David Mumford, Yun Gao, Elie Bienenstock, and John P. Donoghue. Modeling and decoding motor cortical activity using a switching kalman filter. *IEEE Transactions on Biomedical Engineering*, 51(6):933–942, 2004. doi: 10.1109/TBME.2004.826666.
- Friedemann Zenke and Surya Ganguli. Superspike: Supervised learning in multilayer spiking neural networks. *Neural Computation*, 30(6):1514–1541, 2018. doi: 10.1162/neco\_a\_01086.
- Friedemann Zenke and Tim P. Vogels. The remarkable robustness of surrogate gradient learning for instilling complex function in spiking neural networks. *Neural Computation*, 33(4):899–925, 2021. doi: 10.1162/neco\_a\_01367.
- Friedemann Zenke, Ben Poole, and Surya Ganguli. Continual learning through synaptic intelligence. In *Proceedings of the 34th International Conference on Machine Learning (ICML 2017)*, volume 70 of *Proceedings of Machine Learning Research*, pp. 3987–3995, 2017.

## LLM USAGE DISCLOSURE

Large language models (LLMs) were used in this work in following ways. Draft text for all sections, figure captions, and code for experiments/analysis were initially generated with LLM assistance and then edited, verified, and curated by the authors. The authors are solely responsible for the accuracy of all statements, correctness of code, and validity of results.

**Human verification & responsibility.** All claims, equations, proofs/derivations, and references were checked by the authors; all experiments were re-run by the authors from clean environments; and all plots/tables were regenerated from verified outputs.

**Confidentiality & ethics.** No confidential third-party material (e.g., peer reviews, private manuscripts) was provided to any LLM. We did not include hidden prompt-injection text in the submission. All external data/code obeys their licenses, and references were verified to correspond to real, relevant sources.

This disclosure is mirrored in the submission form as required by ICLR policy.

## A EXPERIMENTAL METHODS

We evaluate the Online SNN decoder as follows. Before assessing the continuous online adaptation capabilities of the proposed Online SNN in simulated closed-loop scenarios, we first establish its fundamental decoding efficacy in a more controlled, offline setting. This offline evaluation: 1) allows for comparison against established batch-trained decoders using standardized datasets and metrics, 2) validates the core learning mechanisms of the Online SNN by demonstrating its ability to learn complex neural-to-behavioral mappings from static datasets, and 3) provides a baseline performance characterization before introducing the complexities of closed-loop interaction and non-stationarities. The experimental protocol—encompassing data splitting, preprocessing, training procedures, and evaluation metrics—is kept consistent across all models to ensure fair and unbiased comparisons.

### A.1 DATASETS AND PREPROCESSING

To ensure robust, generalizable findings, we evaluate the decoders on two distinct, publicly available non-human primate intracortical recording datasets (Churchland & Kaufman, 2022; O’Doherty et al., 2017). Both datasets are made available under permissive licenses: the MC Maze dataset is available through DANDI under CC-BY-4.0, and the Zenodo Indy dataset is available under CC-BY-4.0 license. The choice of these datasets is motivated by their widespread use in the BCI research community, the richness of the neural data they provide, and the different behavioral tasks they represent, thereby testing the adaptability of our model to varied neural encoding schemes.

**MC Maze Dataset** This dataset, from the Neural Latents Challenge 2023, contains intracortical multi-unit recordings from a macaque performing a 2D maze navigation task. Its inclusion is valuable due to its recency and the complexity of the continuous control task. Data are accessed using standard neurodata format utilities. Raw neural and kinematic data are initially resampled to a 10 ms resolution. For each trial, data are aligned to movement onset; kinematics are lagged by 80 ms relative to spikes, following the dataset authors’ recommendation for best decode performance. Within each aligned trial, continuous data streams (spikes and hand velocity) are binned into 100 ms windows with a 10 ms stride. The spike input for each 100 ms window is represented by the raw summed spike count from each neuron. True hand-velocity targets ( $v_x, v_y$ ) are derived by numerically differentiating the cursor position data and then averaging the velocity values within each 100 ms window. These target velocities are z-score normalized using statistics derived solely from the training set to prevent data leakage and ensure that the model learns from a standardized output distribution. For the Online SNN evaluation, spike inputs remain as raw counts and are unnormalized. For the Kalman Filter and LSTM models, spike counts are converted to rates (counts per second by dividing by the 100 ms bin width) and then z-score normalized using training set statistics. Data splitting is performed on entire trials (70%/15%/15% for train/validation/test) to prevent temporal correlations from leaking between sets, ensuring a more rigorous evaluation of generalization.

**Zenodo Indy Reaching Dataset** This dataset comprises multi-unit spiking activity from a primate performing center-out reaching movements, a classic BCI paradigm. Its inclusion allows comparison with a large body of existing literature. Raw spike times are loaded directly from data files. Spike events are binned into 50 ms non-overlapping windows, with each window encoded by the raw spike counts from each neuron. To derive cursor velocity, the raw cursor position data is first smoothed using a 4th-order, 10Hz low-pass Butterworth filter, consistent with standard practices for this dataset. The filtered position is then numerically differentiated, and the resulting velocity is mean-averaged within each 50 ms window. A zero-millisecond kinematic lag is used, meaning neural activity and cursor velocity are aligned to the same time bin. Target velocities are z-score normalized using training set statistics. For the Online SNN evaluation, spike features remain as raw counts and are unnormalized. For the Kalman Filter and LSTM models, spike counts are converted to rates (counts per second) and then z-score normalized using training set statistics. Data are split chronologically: the initial 70% of the session’s data is used for training, the subsequent 15% for validation, and the final 15% for testing. This chronological split better reflects a real-world scenario where a decoder is trained on past data and tested on future, unseen data within the same recording session.

## A.2 DECODER ARCHITECTURES AND TRAINING PROCEDURES

The **Online SNN** can be evaluated in two distinct modes:

**Batched Online SNN:** For offline evaluation on static datasets, this mode processes data in fixed-length, overlapping sequences (10 timesteps with 50% overlap, creating sequences at timesteps 0-9, 5-14, 10-19, etc.) grouped into mini-batches. The overlapping design ensures temporal continuity while enabling efficient batch processing, and the 10-timestep length provides sufficient context for short-term temporal dependencies without excessive computational overhead.

**Timestep-wise Online SNN:** For analyzing real-time adaptation, this mode processes data one timestep at a time, with hidden states persisting chronologically to mimic continuous BCI operation. This directly simulates a live, sample-by-sample decoding scenario. State resets can be applied at logical breaks (e.g., trial boundaries). This mode of the Online SNN can be trained for a fewer number of epochs due to the per-timestep updates.

This distinction helps understand the model’s behavior in different deployment contexts. Our hypothesis is that this online, local, and biologically-inspired learning mechanism can achieve competitive performance. It offers advantages in adaptability and computational efficiency.

All neural network decoders (LSTM, BPTT SNN, Online SNN) are implemented in PyTorch and `snnTorch`. Training and evaluation are conducted using a consistent data processing pipeline.

We evaluate the Online SNN’s adaptive capabilities through closed-loop BCI simulations using synthetically generated neural data. Details of the simulation methodology are provided in Appendix H.

## B LEARNING ALGORITHM DETAILS

This appendix provides the complete derivations and implementation details for the three-component learning system introduced in Section 2.2.

### B.1 ELIGIBILITY TRACES

To enable credit assignment over recent activity and to bridge the gap between instantaneous three-factor updates and long-term consolidation, we maintain two sets of eligibility traces for each synaptic weight matrix: a fast trace ( $E^{\text{fast}}(t)$ ) and a slow trace ( $E^{\text{slow}}(t)$ ). These traces accumulate the instantaneous three-factor updates and decay exponentially over time, reflecting a form of working memory for synaptic plasticity (Bellec et al., 2020; Zenke & Ganguli, 2018; Frémaux & Gerstner, 2016). While related to the traces in e-prop, which are derived to approximate BPTT gradients, our traces are implemented as direct, hardware-friendly exponential moving averages of three-factor products rather than as surrogates for a gradient computation. Conceptually, the evolution of an eligibility trace  $E$  is governed by a first-order differential equation:

$$\tau_e \frac{dE}{dt} = -E + \Delta W^{\text{hebb}}$$

<p><b>Algorithm 1:</b> Per-Timestep Online Update</p> <p><b>Input:</b> Spikes <math>\mathbf{x}_t</math>, target velocity <math>\mathbf{y}_t</math></p> <p><b>State:</b> Weights <math>W</math>, membrane potentials <math>\mathbf{u}(t)</math>, traces <math>E^{\text{fast}}, E^{\text{slow}}</math></p> <hr/> <ol style="list-style-type: none"> <li>1. <b>Forward pass:</b> <math>\mathbf{u}(t) \leftarrow \beta \mathbf{u}(t-1) + W \mathbf{x}(t)</math>; get <math>\hat{\mathbf{y}}_t, d_{\text{LIF}}</math></li> <li>2. <b>Error computation:</b> <math>\mathbf{e}(t) \leftarrow \mathbf{y}(t) - \hat{\mathbf{y}}(t)</math></li> <li>3. <b>RMS normalization:</b> Update integer EMAs; <math>\tilde{\mathbf{e}}(t) \leftarrow \mathbf{e}(t) \cdot \text{LUT}[\text{RMS}]</math></li> <li>4. <b>Three-factor term:</b> <math>\Delta W^{\text{hebb}}(t) \leftarrow (\tilde{\mathbf{e}}(t) \odot d_{\text{LIF}}(t))(\text{pre}_t)^T</math></li> <li>5. <b>Update traces:</b> <math>E^{\text{fast}} \leftarrow \lambda_f E^{\text{fast}} + \Delta W^{\text{hebb}}(t)</math></li> <li>6. <math>E^{\text{slow}} \leftarrow \lambda_s E^{\text{slow}} + \Delta W^{\text{hebb}}(t)</math></li> <li>7. <b>Combined trace:</b> <math>E^{\text{comb}} \leftarrow \alpha_{\text{mix}} E^{\text{fast}} + (1 - \alpha_{\text{mix}}) E^{\text{slow}}</math></li> <li>8. <b>Fast update:</b> <math>W \leftarrow W + \eta_{\text{fast}} E^{\text{comb}}</math></li> <li>9. <b>Accumulate:</b> <math>G \leftarrow \mu G + (1 - \mu) E^{\text{comb}}</math></li> <li>10. <b>if</b> <math>t \bmod K = 0</math>: <math>W \leftarrow W + \eta_{\text{slow}} \cdot \mathcal{R}(G)</math></li> <li>11. Update meta multipliers; apply weight decay</li> </ol> <hr/> <p><b>Memory:</b> <math>O(1)</math> in sequence length (weights + 2 traces + stats)</p> <p><b>Compute:</b> <math>O(N^2)</math> per timestep, no backprop graph storage</p>
---

Figure 6: Complete per-timestep update procedure showing  $O(1)$  memory scaling.

where  $\tau_e$  is the trace time constant and  $\Delta W^{\text{hebb}}$  is the instantaneous three-factor update. The discrete update rules, applied at each time step  $t$ , are:

$$E^{\text{fast}}(t) = E^{\text{fast}}(t - \Delta t) \cdot e^{-\Delta t / \tau_{\text{fast}}} + \Delta W^{\text{hebb}}(t) \quad (2)$$

$$E^{\text{slow}}(t) = E^{\text{slow}}(t - \Delta t) \cdot e^{-\Delta t / \tau_{\text{slow}}} + \Delta W^{\text{hebb}}(t) \quad (3)$$

where  $\tau_{\text{fast}}$  (e.g., 120 ms) and  $\tau_{\text{slow}}$  (e.g., 700 ms) are the time constants for the fast and slow traces respectively. The decay coefficients,  $e^{-\Delta t / \tau}$ , are derived directly from these time constants. (In online mode, these time constants are scaled:  $\tau_{\text{fast}}$  is halved and  $\tau_{\text{slow}}$  is scaled by 0.8 for faster adaptation.) These two timescales allow the system to maintain sensitivity to recent, rapid changes while also preserving a longer-term memory of relevant activity. A combined eligibility trace,  $E^{\text{comb}}(t)$ , is then formed as a linear mixture of the fast and slow traces:

$$E^{\text{comb}}(t) = \alpha_{\text{mix}} \cdot E^{\text{fast}}(t) + (1 - \alpha_{\text{mix}}) \cdot E^{\text{slow}}(t) \quad (4)$$

where  $\alpha_{\text{mix}}$  is a mixing coefficient (e.g., 0.5), which determines the relative influence of the fast and slow eligibility traces. This combined trace is what drives the effective fast weight updates applied to the network at each timestep:

$$\Delta W(t) = \eta_{\text{fast}} \cdot E^{\text{comb}}(t),$$

where  $\eta_{\text{fast}}$  is the fast learning rate that scales immediate, per-timestep plastic changes. It controls the responsiveness of the working weights to the most recent activity and error and is adapted online by the meta-learning rule introduced below.

## B.2 TWO-TIMESCALE WEIGHT CONSOLIDATION

Online learning systems must balance plasticity and stability, especially in non-stationary environments like BCIs: the system must be plastic enough to adapt to new information or changes in input statistics, yet stable enough to retain previously learned knowledge. To address this, our model incorporates a two-timescale weight consolidation mechanism. This approach is inspired by biological theories of memory consolidation, where learning initially induces labile synaptic changes (fast timescale) that are later consolidated into more enduring forms (slow timescale) (Fusi et al., 2005; Benna & Fusi, 2016; Kirkpatrick et al., 2017; Zenke et al., 2017). By maintaining separate fast-changing (transient) and slow-changing (stable) weight components, our system can rapidly respond to immediate errors via the fast Hebbian updates, while gradually integrating persistent changes into the more stable slow weights. This prevents catastrophic forgetting and promotes

long-term learning. The combined eligibility trace  $E^{\text{comb}}(t)$  is accumulated into a momentum-filtered accumulator  $G(t)$ , which smooths out noisy single-timestep updates:

$$G(t) = \mu G(t-1) + (1-\mu)E^{\text{comb}}(t), \quad (5)$$

where  $\mu$  is the momentum coefficient (e.g., 0.9). Periodically (every  $K$  timesteps, where  $K$  is a hyperparameter balancing responsiveness and stability), these accumulated, smoothed changes (represented by  $G(t)$ ) are averaged over the  $K$  timesteps, then normalized by their Root Mean Square (RMS) value using the function  $\mathcal{R}(\cdot)$ , and finally consolidated into the slow weights, which are the weights actually used for inference:

$$W^{\text{slow}}(t+K) = (1-\alpha)W^{\text{slow}}(t) + \alpha \mathcal{R}(\bar{G}_K(t)), \quad (6)$$

where  $\alpha$  is the slow learning rate, and  $\bar{G}_K(t)$  denotes the average of  $G(s)$  over the preceding  $K$  timesteps. The function  $\mathcal{R}(X) = X / (\sqrt{\text{mean}(X^2)} + \epsilon)$  normalizes the gradient by its RMS, ensuring stable updates regardless of gradient magnitude. In this two-rate scheme,  $\eta_{\text{fast}}$  scales instantaneous updates applied continuously through the eligibility pathway, whereas  $\alpha$  (equivalently, a slow step size  $\eta_{\text{slow}}$ ) scales the periodic consolidation that integrates smoothed evidence into the stable weights every  $K$  timesteps. This separation allows rapid, potentially transient adaptations without immediately overwriting the stable substrate, preserving past knowledge while still permitting continuous improvement.

To prevent overfitting, during each slow (consolidative) update, we apply a 1e-5 decay on the weight matrices.

### B.3 META-ADAPTATION OF PLASTICITY

The meta-adaptation mechanism is detailed in the main text. After each consolidation, a light decay is applied and the window statistics are reset to keep the controller responsive to recent performance.

**Reward-Modulated LUT.** For completeness, we note that all Zenodo results reported in this work include a reward-modulated lookup table (LUT) that discretizes the instantaneous output error into 16 integer buckets, each associated with a fixed multiplicative gain for the fast learning rate. This provides a coarse neuromodulatory signal that enhances plasticity when errors are large and suppresses it when errors are small, while remaining hardware-friendly (integer-only, no divisions). Although not central to our theoretical framework, the LUT yielded a measurable gain on Zenodo, improving individual X and Y correlation by approximately 5-10% (from  $\sim 0.597$  to at least  $\sim 0.63$ ). On MCmaze, the LUT had no significant measurable effect. We therefore regard it as an optional implementation detail rather than a theoretical requirement of the algorithm.

### B.4 STABILITY AND HOMEOSTASIS

Continuous online learning, especially with three-factor rules that reinforce correlated activity, can be prone to instabilities such as runaway synaptic weights or saturated neuronal activity. To ensure stable long-term operation, which is necessary for any practical BCI system, our model employs two biologically-inspired homeostatic mechanisms. Homeostatic plasticity refers to the set of processes that neurons and neural circuits use to maintain their electrical activity within a stable physiological range, despite perturbations or ongoing synaptic modifications (Abbott & Nelson, 2000; Turrigiano & Nelson, 2004). These mechanisms are vital for preventing pathological states like epilepsy (runaway excitation) or silent networks (insufficient activity) and are implemented in our model as follows:

1. **Per-Neuron Weight Scaling and Clipping:** After each timestep, the incoming synaptic weights for each individual neuron are scaled and clipped to prevent weight explosion. This mechanism calculates the L2 norm of each row (representing incoming weights to a neuron) and rescales weights that exceed a predefined maximum threshold through power-of-two division operations. This prevents any single neuron’s weights from exploding, thereby maintaining stable total synaptic drive and preventing numerical instability. The power-of-two scaling approach is chosen for hardware efficiency, as it can be implemented using simple bitwise operations on neuromorphic processors.



identical. Zenodo Indy provides continuous, self-paced reaches without explicit trial alignment or standardized neuro-to-kinematic lag. Error signals are temporally broader and less synchronized with presynaptic events. Here  $d_{LIF}$  gates learning to moments when postsynaptic neurons are near threshold, sharpening credit assignment and yielding large gains ( $\Delta R \approx 0.1-0.2$ ).

2) Task and temporal statistics. MC Maze movements are constrained by trial structure and alignment to move onset, producing stereotyped dynamics and smoother velocity trajectories within windows, which makes coarse error-driven updates sufficient. Zenodo Indy includes self-paced reaches to dense target grids, richer kinematic variability, and session-to-session heterogeneity. Sensitivity gating prioritizes updates during informative transients and suppresses updates during quiescent or saturated regimes, improving bias–variance trade-offs under these conditions.

3) Noise and spiking sparsity. Zenodo Indy sessions often include higher unit counts and mixed sorting quality (including unsorted threshold crossings), leading to sparser and noisier effective inputs. The three-factor gate down-weights updates when postsynaptic units are far from threshold (low  $d_{LIF}$ ), mitigating noise amplification that the delta rule would otherwise introduce. MC Maze’s binning plus lag yields higher effective SNR, so the delta rule is already close to optimal.

Empirically, the ablations reflect these factors: on Zenodo Indy, replacing three-factor with delta degrades both axes with statistically significant drops, whereas on MC Maze the difference is negligible. In short,  $d_{LIF}$  confers robustness when timing is less controlled, dynamics are more varied, and spike signals are noisier; when alignment and structure improve effective SNR (as in MC Maze with an 80 ms lag), delta updates suffice.

For MC Maze, the ablations indicate that the three-factor and delta rules perform nearly identically, with differences that are very small and not practically meaningful. Architectural recurrence confers a consistent, modest gain concentrated on Y while X remains similar across architectures, suggesting a limited but reliable contribution from temporal memory. Full RMS normalization provides the strongest results, no normalization is close behind, and partial normalization is noticeably worse; consequently, partial normalization should be avoided. With regard to trace timescales, slow traces are strongest, medium and dual traces are close, and fast traces are weakest, indicating that longer temporal integration is beneficial on this dataset. In terms of update mechanisms, using both fast and slow updates performs best, fast-only is slightly lower, and slow-only or frozen updates collapse performance toward zero, underscoring the necessity of rapid adaptation. Meta-adaptation yields only very small gains on average and is not a primary driver of performance.

## D OVERVIEW OF SPIKING NEURAL NETWORKS

Spiking Neural Networks (SNNs) represent a class of artificial neural networks that more closely emulate the computational principles of biological nervous systems. Unlike traditional artificial neurons that process continuous-valued activations, SNNs employ discrete, event-driven spikes for information transmission and processing. This bio-mimicry is a primary reason for their selection in BCI research, as it offers a potential avenue for energy-efficient computation, especially when deployed on neuromorphic hardware designed to leverage sparse, spike-based communication (Roy et al., 2019; Furber et al., 2014). The canonical Leaky Integrate-and-Fire (LIF) neuron model, a common choice for SNNs due to its computational simplicity and biological relevance, describes the evolution of a neuron’s membrane potential  $u(t)$  as:

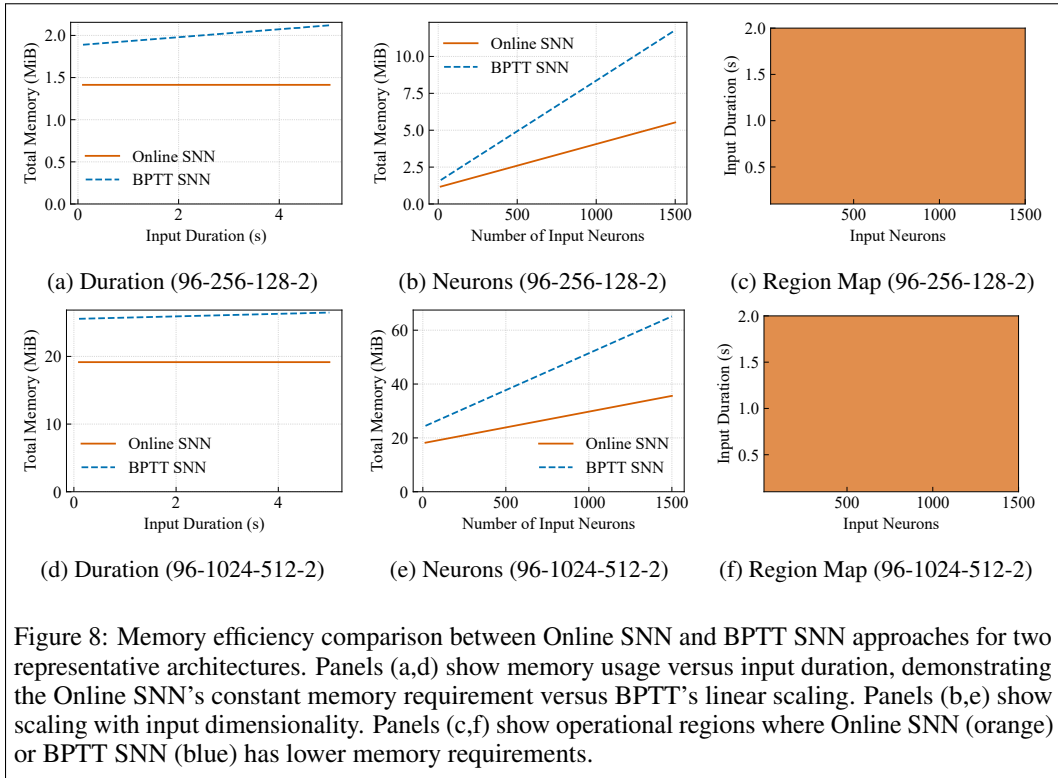
$$\tau_m \frac{du(t)}{dt} = -(u(t) - u_{\text{rest}}) + RI(t),$$

where  $\tau_m$  is the membrane time constant,  $u_{\text{rest}}$  the resting potential,  $R$  the input resistance, and  $I(t)$  the synaptic input current. When  $u(t)$  exceeds a threshold  $u_{\text{th}}$ , the neuron emits a spike, and  $u(t)$  is reset to  $u_{\text{reset}}$ . This event-driven nature can significantly reduce computational load if spikes are sparse.

SNNs are often trained using learning rules inspired by neurobiology, such as Spike-Timing-Dependent Plasticity (STDP). STDP is a form of Hebbian learning where the change in synaptic strength (weight) depends on the precise relative timing of pre-synaptic and post-synaptic spikes (Song et al., 2000). Hebbian plasticity, encapsulated by the maxim "cells that fire together, wire together," is a foundational concept in neuroscience, providing a local, activity-dependent, and thus biologically plausible mechanism for synaptic learning (Hebb, 1949; Markram et al., 1997; Bi & Poo,

1998; Caporale & Dan, 2008). Its locality means that weight updates depend only on information available at the synapse, avoiding the need for global error signals or complex backward computations characteristic of algorithms like backpropagation. This makes Hebbian-like rules attractive for online, adaptive systems where computational resources are limited, and biological realism is desired. While pure STDP can learn temporal correlations, its application to supervised tasks like BCI decoding often requires modulation by reward or error signals, leading to three-factor learning rules, which our work builds upon. The challenge with direct application of traditional spike-based learning rules on conventional hardware can be the substantial computational and memory overhead for tracking precise spike times and managing complex plasticity dynamics, motivating our development of an efficient, online SNN learning algorithm.

### E MEMORY EFFICIENCY ANALYSIS



Our Online SNN approach has a reduced memory footprint compared to SNNs trained with Backpropagation Through Time (BPTT). This matters for implantable BCIs, which face strict power and memory constraints. The fundamental difference lies in how each approach handles memory allocation during training and inference.

**Memory Calculation Methodology** We categorize memory usage into static and dynamic components. Static memory includes all data structures that remain constant regardless of input sequence length, while dynamic memory scales with temporal sequence duration.

For the **Online SNN**, memory requirements consist entirely of static components:

- **Network parameters:** All synaptic weights and biases across the three-layer architecture
- **Eligibility traces:** Two sets of trace matrices (fast and slow) that maintain the same dimensions as the corresponding weight matrices
- **Homeostatic variables:** Running statistics for RMS normalization, which scale with network width rather than sequence length

The total parameter count includes: input-to-hidden connections, recurrent hidden-to-hidden connections, hidden-to-hidden connections between layers, and hidden-to-output connections, plus all

associated biases. Each parameter requires storage in single-precision floating-point format (4 bytes). The eligibility traces double this requirement, as both fast and slow traces mirror the parameter structure. Therefore, Online SNN memory scales as three times the base parameter count (parameters plus two trace sets).

For the **BPTT SNN**, memory requirements include both static and dynamic components. **Static memory**: Network parameters, gradient buffers (same size as parameters), and optimizer state variables (Adam requires two additional buffers per parameter (Kingma & Ba, 2015)). **Dynamic memory**: Computational graph storage for backpropagation, including intermediate activations (hidden states, membrane potentials), spike outputs, and gradient flow information across the temporal sequence used by automatic differentiation.

The static memory for BPTT scales as four times the base parameter count (parameters, gradients, and two Adam optimizer state buffers). The dynamic memory grows linearly with sequence length, as each timestep requires storage of layer activations, membrane states, spike outputs, and intermediate computational results needed for gradient computation through the temporal unfolding.

**Quantitative Analysis** We provide detailed analysis for two representative architectures: (a) 96-256-128-2 and (b) 96-1024-512-2, where the format represents input-hidden1-hidden2-output neuron counts. For a standard 120-timestep sequence (corresponding to 1.2 seconds of neural data at 100 Hz), the memory breakdown is shown in Table 2.

For the smaller architecture (96-256-128-2), the Online SNN requires 1.41 MB while the BPTT SNN requires 2.17 MB at peak usage, representing a 35.0% memory reduction. For the larger architecture (96-1024-512-2), the Online SNN requires 19.15 MB compared to BPTT’s 26.67 MB, achieving a 28.2% memory reduction.

The dynamic memory component for BPTT is calculated through empirical measurement of the computational graph overhead during backpropagation. This measurement captures the memory required to store intermediate activations and gradients throughout the temporal sequence. The dynamic memory scales approximately linearly with both sequence length and total network width (sum of all hidden layer sizes).

**Scaling Properties** The memory advantage of the Online SNN becomes more pronounced for longer sequences, as illustrated in Figure 8. While BPTT memory usage increases linearly with input duration due to the growing computational graph, Online SNN memory remains constant regardless of sequence length. This fixed memory characteristic makes the Online SNN suitable for continuous, long-duration BCI operation where sequences can extend for minutes or hours without interruption.

The analysis reveals that for typical BCI applications involving continuous neural decoding over extended periods, the Online SNN’s fixed memory footprint provides advantages over BPTT-based approaches. This memory efficiency, combined with avoiding computational graph storage and gradient accumulation, enables deployment on resource-constrained neuromorphic hardware platforms designed for implantable BCI systems (Basu et al., 2022; Hasler & Basu, 2025).

## F BACKGROUND ON LEARNING RULES AND PLASTICITY

### F.1 THREE-FACTOR LEARNING RULES AND ELIGIBILITY TRACES

Modern biologically plausible learning in SNNs builds upon classical Hebbian plasticity but extends it with three-factor learning rules that incorporate an additional modulatory signal (Frémaux & Gerstner, 2016; Kusmierz et al., 2017; Seung, 2003; Izhikevich, 2007; Florian, 2007; Mozafari et al., 2018). Classical spike-timing-dependent plasticity (STDP) represents a two-factor Hebbian rule based on pre- and postsynaptic spike coincidences. However, three-factor learning rules incorporate a third factor—such as a neuromodulator, reward signal, or error feedback—that provides global context to guide synaptic changes. This third factor enables superior credit assignment and adaptation in SNNs, bridging the gap between neuroscience and machine learning perspectives (Mazurek et al., 2025).

A key innovation for biologically plausible credit assignment is the introduction of *eligibility traces*—transient memory variables that accumulate local pre/post activity influence over time

(Bellec et al., 2020; Zenke & Ganguli, 2018). These traces decay like synaptic "footprints" of recent activity and are later modulated by a third factor (error or reward) to effect weight changes. This forms the basis of algorithms like e-prop (eligibility propagation) and SuperSpike. Bellec et al. demonstrated that e-prop, which uses ODE-inspired decaying traces, can train recurrent SNNs online with performance close to backpropagation-through-time (Bellec et al., 2020). Similarly, Zenke & Ganguli’s SuperSpike derived a voltage-based three-factor rule for multilayer SNNs, showing that purely local spike traces combined with a global error signal can train multilayer networks (Zenke & Ganguli, 2018).

Crucially, these approaches perform online updates: the network does not need to be unfolded in time, avoiding the high memory costs associated with BPTT. The role of eligibility traces is supported by neuroscience—neurons are believed to maintain biochemical traces of pre/post spike pairings that remain dormant until a top-down signal (e.g., dopamine burst) arrives (Frémaux & Gerstner, 2016; Seung, 2003; Izhikevich, 2007). In effect, surrogate gradient algorithms with eligibility traces implement biologically inspired credit assignment: local Hebbian accumulation of potential changes, gated by a global factor when a learning signal occurs.

## F.2 DUAL TIMESCALES AND META-PLASTICITY

Biological synapses exhibit multiple timescales of plasticity—fast changes that capture recent events and slower processes for long-term stability (Benna & Fusi, 2016; Zenke et al., 2017). Many SNN learning models mirror this by employing dual timescale traces or learning rates. For instance, modern implementations maintain both "fast" and "slow" eligibility traces, reminiscent of the triplet STDP model that used separate decay constants for different spike interactions (Pfister & Gerstner, 2006). Neuromorphic hardware platforms like Intel’s Loihi chip explicitly support this architecture, offering multiple filtered spike traces per synapse with short and long time constants, enabling rules that combine precise spike-timing effects with longer-term rate-based effects (Davies et al., 2018).

The interplay of fast and slow components represents a form of meta-plasticity, where one plasticity process modulates another. Benna and Fusi’s synaptic memory model argued that coupling fast and slow weight variables can greatly extend memory lifetime (Benna & Fusi, 2016). Likewise, research has shown that fast updates combined with slower weight stabilization mechanisms improve continual learning (Zenke et al., 2017; Kirkpatrick et al., 2017).

Beyond hardwired timescales, researchers have begun exploring meta-learning of plasticity rules themselves. Recent work has used bi-level optimization to train SNNs that adapt their own synaptic update rules over time (Schmidgall et al., 2023). Such meta-plastic SNNs can adjust how they learn in response to experience, echoing the brain’s ability to regulate plasticity via neuromodulators or gene expression changes. Incorporating dual timescales and meta-plasticity is increasingly recognized as key to robust online learning in spiking networks.

## G ABLATION STUDY DESIGN

To evaluate each component’s contribution within the Online SNN’s learning rule, we conduct several ablation studies. These compare the full model to variants where specific components are removed or modified. The experimental setup for these studies is otherwise kept consistent with the main offline evaluation.

This study isolates the contribution of the three-factor learning mechanism by comparing the full Online SNN with a variant where the neuronal sensitivity term is removed. Specifically, we compare the full three-factor rule (Equation 1) against a simplified delta rule that eliminates the surrogate gradient term:

$$\Delta W_{ij}^{\text{delta}}(t) = e_j(t) \text{pre}_i(t) \tag{Delta Rule}$$

This delta rule ablation removes the neuronal sensitivity gating ( $d_{\text{LIF}}$ ) while maintaining the error-driven and activity-dependent components. The update rule in this ablated version effectively reduces to a basic error-driven change, proportional only to the error signal without local neuron sensitivity modulation. We also investigate the impact of the adaptive meta-learning mechanism, which dynamically adjusts the fast and slow learning rates based on recent performance. This variant compares the full model against a version where the learning rates are kept fixed at their base values

throughout training, without any meta-adaptation. This ablation assesses the importance of recurrent connections within the SNN; the full recurrent network is compared to a feedforward-only variant, where the recurrent input to the first hidden layer is removed, and information flows strictly in one direction. Furthermore, we examine the role of different temporal integration windows for the eligibility traces, which accumulate weight updates over time, by comparing the full model’s dual-timescale traces (combining fast and slow decay components) against variants using only a fast timescale (shorter memory), only a slow timescale (longer memory), or a single intermediate timescale. Finally, we investigate the effect of normalizing error signals and neuronal activities by their root-mean-square (RMS) values during the update process, comparing the full model with RMS normalization against versions with partial RMS normalization (e.g., only on the output error) and no RMS normalization at all.

For ablation analysis and statistical testing, each configuration produces per-session Pearson correlations for the X and Y velocity components. For plotting, the aggregate statistic shown for each configuration and axis is the across-session mean, with error bars reflecting a normal-approximation 95% confidence interval computed as  $\pm 1.96$  times the standard error of the mean, where the standard deviation uses the unbiased estimator with degrees of freedom equal to one less than the number of sessions. Significance annotations are derived from paired, two-sided t-tests across sessions that compare a designated baseline configuration to each alternative within the same ablation family, performed separately for X and for Y. Pairing is enforced by aligning on the intersection of sessions that contain measurements for both configurations; comparisons with fewer than two paired observations are omitted. Significance thresholds use the following convention:  $p < 0.001$  is annotated with three stars,  $p < 0.01$  with two stars,  $p < 0.05$  with one star, and  $p \geq 0.05$  is marked as not significant. No multiple-comparisons correction is applied, as tests are presented as descriptive indicators alongside effect direction inferred from the plotted means. Baselines are chosen per family: for trace timescale comparisons, a canonical ordering defines which configuration is treated as the baseline; for update-mechanism comparisons, the dual-update configuration serves as the baseline. When update-mechanism analyses require a dual baseline that is not present in the current results table, the dual baseline is drawn from the corresponding trace-timescale results and paired only on sessions common to both sources, preserving the within-session design. Configuration labels may be harmonized to canonical names before analysis to ensure consistent grouping across files. The visualizations present grouped bars for X and Y per configuration on a common vertical scale from zero to slightly above one to include the confidence intervals.

## H CLOSED-LOOP SIMULATION METHODS

To further evaluate the adaptive capabilities of the Online SNN, particularly in dynamic environments, we conducted a series of online closed-loop BCI simulations using synthetically generated neural data. Closed-loop simulation is an important validation approach for BCI systems, as demonstrated by Cunningham et al. (Cunningham et al., 2011), who showed that offline analyses can be misleading and that closed-loop testing reveals fundamentally different optimal parameters than offline evaluation. Their work demonstrated that while offline analyses suggested optimal Kalman filter bin widths of 100-300ms, closed-loop testing with human subjects revealed that much shorter bin widths (25-50ms) yielded superior decode performance when feedback control was incorporated. This finding was subsequently confirmed in closed-loop rhesus monkey experiments, establishing that closed-loop simulation is necessary for understanding the role of feedback control and co-adaptation between the user and decoder (Cunningham et al., 2011). These simulations model how decoder outputs continuously influence the system state and subsequent neural inputs. This reflects the sequential dependencies and error characteristics in real BCI operation that cannot be captured through static offline analysis. This section details the methodology for these simulations. We investigate two distinct closed-loop simulation protocols: one for assessing adaptation to neural disruptions and another for evaluating online learning from scratch.

### H.0.1 SYNTHETIC NEURAL DATA GENERATION

We simulate a 2D cursor control task using a synthetic neural population comprising 96 neurons with cosine-tuned directional preferences. Each neuron  $i$  has a preferred direction  $\mathbf{d}_i \in \mathbb{R}^2$  with unit norm, distributed uniformly across four quadrants to ensure balanced directional representation.

Given a target velocity  $\mathbf{v}(t) \in \mathbb{R}^2$  at timestep  $t$ , the firing rate for neuron  $i$  is computed as:

$$r_i(t) = r_{\min} + (r_{\max} - r_{\min}) \cdot \max\left(0, \frac{\mathbf{d}_i \cdot \hat{\mathbf{v}}(t) + 0.5}{1.5}\right) \quad (7)$$

where  $\hat{\mathbf{v}}(t) = \mathbf{v}(t) / (2.0 \cdot \|\mathbf{v}(t)\|)$  is the scaled velocity,  $r_{\min} = 5$  Hz and  $r_{\max} = 100$  Hz are the minimum and maximum firing rates, respectively. When  $\|\mathbf{v}(t)\| = 0$ , we set  $\hat{\mathbf{v}}(t) = \mathbf{0}$  to avoid division by zero.

The spike probability for neuron  $i$  is then:

$$p_i(t) = \text{clamp}(r_i(t) \cdot \Delta t + \mathcal{N}(0, \sigma^2), 0, 1) \quad (8)$$

where  $\Delta t = 0.01$  s is the timestep duration,  $\sigma = 0.02$  is the noise standard deviation, and  $\mathcal{N}(0, \sigma^2)$  represents Gaussian noise. Finally, binary spikes are generated as  $s_i(t) \sim \text{Bernoulli}(p_i(t))$ .

### H.0.2 TASK STRUCTURE FOR CLOSED-LOOP SIMULATION

The experimental paradigm involves a sequence of 2D center-out reach tasks on a simulated screen of dimensions 800x600 units. At each trial, a target is positioned at coordinates  $(x_{\text{target}}, y_{\text{target}})$  with distance constraint  $\|\mathbf{p}_{\text{target}} - \mathbf{p}_{\text{center}}\| > 3R$  from the center position  $\mathbf{p}_{\text{center}} = [400, 300]^T$ , where  $R = 50$  units is the target radius.

The closed-loop control dynamics operate as follows. At each timestep  $t$ , the desired velocity is computed using a proportional controller:

$$\mathbf{v}_{\text{desired}}(t) = \frac{\mathbf{p}_{\text{target}} - \mathbf{p}_{\text{cursor}}(t)}{\|\mathbf{p}_{\text{target}} - \mathbf{p}_{\text{cursor}}(t)\|} \cdot \min\left(1.0, \frac{\|\mathbf{p}_{\text{target}} - \mathbf{p}_{\text{cursor}}(t)\|}{200}\right) \quad (9)$$

where  $\mathbf{p}_{\text{cursor}}(t)$  is the current cursor position. This desired velocity drives the synthetic neural population to generate spikes  $\mathbf{s}(t)$  according to Equations (7-8).

The decoder processes these spikes to produce an estimated velocity  $\hat{\mathbf{v}}_{\text{decoder}}(t)$ , which updates the cursor position:

$$\mathbf{p}_{\text{cursor}}(t+1) = \text{clamp}(\mathbf{p}_{\text{cursor}}(t) + \alpha \cdot \hat{\mathbf{v}}_{\text{decoder}}(t), [0, 800] \times [0, 600]) \quad (10)$$

where  $\alpha = 5$  is the movement scaling factor. Success occurs when  $\|\mathbf{p}_{\text{target}} - \mathbf{p}_{\text{cursor}}(t)\| < R$  within 300 timesteps (3 seconds).

### H.0.3 EXPERIMENTAL PROTOCOLS AND PHASES

**Online Adaptation and Disruption Ablations** Each experimental run in this protocol is structured into two phases to assess performance before and after a controlled neural perturbation. Decoders are evaluated in matched conditions but not with identical spike sequences at the same timestamps.

**Phase 1: Initial Learning (Pre-Disruption):** All decoders (KF, LSTM, BPTT SNN) first undergo an initial calibration phase using a dataset of 10,000 synthetically generated spike-velocity steps. The KF parameters are estimated via maximum likelihood, while LSTM and BPTT SNN undergo offline training.

This dataset was generated using a closed-loop methodology to better reflect interactive BCI dynamics. An open-loop alternative (spikes from idealized trajectories) was considered but does not capture how decoder outputs influence future inputs and errors.

To enhance ecological validity, the 10,000-step dataset for calibrating the Kalman Filter, LSTM, and BPTT SNN was generated in closed loop. An untrained LSTM drove the cursor; at each timestep, the ideal velocity to target was recorded as the label, spikes were generated from that ideal velocity, and the untrained LSTM's output advanced the cursor. This yielded data collected under decoder-driven trajectories with realistic sequential dependencies. The KF parameters were estimated from this dataset, while LSTM and BPTT SNN were trained in a supervised manner before evaluation.

In this protocol, the Online SNN was pre-trained through 100 closed-loop reach attempts to establish an initial functional state. Following this training, all decoders were evaluated over 150 successful reach trials using the unperturbed spike generator with baseline noise and tuning.

**Phase 2: Adaptation to Disruption:** Immediately following Phase 1, a specific disruption is introduced to the spike generator’s properties. Three types of disruptions are investigated in separate experiments:

**Remapping:** For intensity  $\lambda \in [0, 1]$ , a fraction  $\min(0.95, 1.9\lambda)$  of neurons have their preferred directions reassigned. For selected neuron  $i$ , new preferred directions are computed as:

$$\mathbf{d}_i^{\text{new}} = [\cos(\theta_i^{\text{new}}), \sin(\theta_i^{\text{new}})]^T \quad (11)$$

where  $\theta_i^{\text{new}} = \text{Uniform}(0, 2\pi) + \text{Bernoulli}(0.5) \cdot \pi$  to create dramatic directional shifts.

**Drift:** Firing rate parameters are modified as:

$$r_{\text{max}}^{\text{new}} = r_{\text{max}}^{\text{orig}} \cdot (1.0 - 1.6\lambda) \quad (12)$$

$$r_{\text{min}}^{\text{new}} = r_{\text{min}}^{\text{orig}} \cdot (1.0 + 6\lambda) \quad (13)$$

Additionally, noise variance increases with a capped schedule:  $\sigma^{\text{new}} = \min(0.4, \sigma^{\text{orig}} \cdot (1 + 4\lambda))$ .

**Dropout:** A fraction  $\min(0.9, 1.8\lambda)$  of neurons are silenced by applying a binary mask  $\mathbf{m} \in \{0, 1\}^{96}$  to the spike output:  $\mathbf{s}_{\text{masked}}(t) = \mathbf{s}(t) \odot \mathbf{m}$ .

After disruption onset, all decoders were evaluated on an additional 50 reach trials. During this phase, only the Online SNN continued to adapt its weights online; the KF, LSTM, and BPTT SNN operated with fixed weights from the initial offline training.

**No-Pretrain / Online-Only Calibration Comparison** To investigate decoder capability to learn from scratch and compare online versus offline calibration, a separate experimental protocol is employed. In **Phase 1: Online Data Collection & Online SNN Adaptation**, all decoders (KF, LSTM, BPTT SNN, Online SNN) are initialized with random weights (or default parameters for KF). Each decoder then controls the cursor for 30 reach attempts. During these trials, the Online SNN actively adapts its weights based on ongoing performance. The other decoders (KF, LSTM, BPTT SNN) operate with fixed random weights, solely for the purpose of collecting a diverse set of spike-velocity data under their respective (initially poor) control policies. Data from each decoder’s interaction (spike trains and ideal velocities) are stored separately. Following Phase 1, in **Phase 2: Post-Calibration Evaluation**, the offline-trainable decoders (KF, LSTM, BPTT SNN) are trained (calibrated) using only the data they respectively collected during their 30 interaction trials in Phase 1. The Online SNN carries forward the weights learned during its Phase 1 online adaptation. Subsequently, all four decoders are evaluated on a new set of 70 reach trials.

#### H.0.4 OFFLINE TRAINING HYPERPARAMETERS

#### H.0.5 EVALUATION METRICS FOR CLOSED-LOOP SIMULATIONS

Decoder performance is primarily quantified by **Time to Reach Target (seconds)**- For each successful reach, the number of 10ms timesteps taken to acquire the target is recorded. This is converted to seconds for reporting. Timeouts (reaching the 3-second limit) are assigned the maximum duration.

The **Mean and Standard Error of the Mean (SEM) of Reach Times** are computed across 10 independent experimental runs, each initiated with a different random seed, to account for stochasticity in target placement, spike generation, and model initializations. Learning curves plot the smoothed (rolling mean, window N=15) time to reach target across consecutive trials.

#### H.0.6 IMPLEMENTATION DETAILS FOR CLOSED-LOOP SIMULATIONS

All experiments are conducted using custom simulation scripts leveraging PyTorch, snnTorch, NumPy, and Matplotlib. The simulation environment is structured to ensure reproducibility, with controlled random seeds for all stochastic processes. The synthetic environment and decoder evaluations are performed within a consistent simulation loop ensuring fair comparisons. Decoders are evaluated separately in individual reach attempts, not concurrently with identical spike data.

Table 3: Complete hyperparameters for offline SNN training on MC Maze and Zenodo datasets.

Parameter	MCMaze Batched On-line SNN	MCMaze True Online SNN	Zenodo Batched On-line SNN	Zenodo True Online SNN
<i>Architecture</i>				
Input size	182	182	96	96
Hidden layer 1	1024	1024	256	256
Hidden layer 2	512	512	128	128
Output size	2	2	2	2
Recurrent connections	Yes (layer 1)	Yes (layer 1)	Yes (layer 1)	Yes (layer 1)
<i>Data Processing</i>				
Bin width	100ms	100ms	50ms	50ms
Stride	10ms	10ms	50ms	50ms
Kinematic lag	80ms	80ms	0ms	0ms
Spike processing	Count	Count	Count	Count
Normalization	None	None	None	None
<i>Neuron Parameters</i>				
Surrogate gradient	Fast sigmoid	Fast sigmoid	Fast sigmoid	Fast sigmoid
LIF $\beta$ (layers 1,2)	0.7, 0.7	0.7, 0.7	0.7, 0.7	0.7, 0.7
LIF $\beta$ (output)	0.5	0.5	0.5	0.5
LIF threshold	1.0	1.0	1.0	1.0
Reset mechanism	None (output)	None (output)	None (output)	None (output)
<i>Learning Parameters</i>				
Fast learning rate	$1 \times 10^{-5}$	$1 \times 10^{-4}$	$3 \times 10^{-3}$	$2 \times 10^{-3}$ (adaptive)
Slow learning rate	$1 \times 10^{-6}$	$1 \times 10^{-5}$	$1 \times 10^{-3}$	$2 \times 10^{-4}$
Meta learning rate	0.01	0.01	0.01	0.01
$\tau_{fast}$	120ms	120ms	120ms	120ms
$\tau_{slow}$	700ms	700ms	700ms	700ms
Trace mixing $\alpha_{mix}$	0.5	0.8	0.5	0.8
Window size $K$	50	200	50	50
Momentum $\mu$	0.9	0.9	0.9	0.9
Weight decay	$1 \times 10^{-5}$	$1 \times 10^{-5}$	$1 \times 10^{-5}$	$1 \times 10^{-5}$
Weight cap $c_\ell$	6.0	6.0	6.0	6.0
<i>Training</i>				
Epochs (disregarding early stopping)	20	3 (due to high data volume for single timestep)	20	20 (low data volume for single timestep)
Batch size	32	1	32	1
Sequence length	10	1	10	1
Patience	10	8	10	20
Eval frequency	each epoch	1000 steps	each epoch	500 steps
State reset	trial bound.	trial bound.	N/A	200 steps

Table 4: Hyperparameters for baseline decoders (LSTM and Kalman Filter) on MC Maze and Zenodo datasets.

Parameter	MC Maze LSTM	Zenodo LSTM	MC Maze KF	Zenodo KF
<i>Architecture</i>				
Input size	182	96	182	96
Hidden units	256	256	N/A	N/A
Layers	2	2	N/A	N/A
Output size	2	2	2	2
Dropout	0.2	0.2	N/A	N/A
<i>Data Processing</i>				
Spike processing	Rate (Hz)	Rate (Hz)	Rate (Hz)	Rate (Hz)
Normalization	Z-score	Z-score	Z-score	Z-score
Sequence length	10 (offline), 5 (online)	10 (offline), 5 (online)	N/A	N/A
<i>State Space (KF only)</i>				
State dimensions	N/A	N/A	2 (velocity)	2 (velocity)
Observation dim.	N/A	N/A	182	96
Process noise Q	N/A	N/A	0.1	0.1
Observation noise R	N/A	N/A	1.0	1.0
Initial covariance P	N/A	N/A	100.0	100.0
<i>Training (Offline)</i>				
Epochs (disregarding early stopping)	50	50	N/A (analytical)	N/A (analytical)
Batch size	64	64	N/A	N/A
Learning rate	$1 \times 10^{-3}$	$1 \times 10^{-3}$	N/A	N/A
Optimizer	Adam	Adam	N/A	N/A
Weight decay	$1 \times 10^{-5}$	$1 \times 10^{-5}$	N/A	N/A
Patience	10	10	N/A	N/A

Table 5: Complete hyperparameters for closed-loop experiments across all protocols and decoders.

Parameter	Adaptation Protocol	No-Pretrain Protocol	BCI Simulation Default Parameters
<i>Neural Population &amp; Environment</i>			
Neural population	96 neurons	96 neurons	96 neurons
Spike generator noise	0.02	0.02	0.02
Screen dimensions	800×600 units	800×600 units	800×600 units
Target radius	50 units	50 units	50 units
Center position	[400, 300]	[400, 300]	[400, 300]
Movement scale	5 units/step/vel	5 units/step/vel	5 units/step/vel
Max reach duration	3.0 seconds	3.0 seconds	10.0 seconds
Disruption intensities	Remap/Drift/Dropout (0.9)	N/A	Remap/Drift/Dropout (0.5)
<i>Task Structure</i>			
Offline pretraining steps	10,000	N/A	10,000
Online SNN pretrain reaches	100	N/A	400
Initial learning reaches	150	N/A	400
Adaptation reaches	50	N/A	120
Online data collection	N/A	30 reaches	N/A
Post-calibration eval	N/A	70 reaches	N/A
<i>SNN Architecture (All Variants)</i>			
Input size	96	96	96
Architecture	96-256-128-2	96-256-128-2	96-512-256-2
Hidden LIF $\beta$	0.7, 0.7	0.7, 0.7	0.7, 0.7
Output LIF $\beta$	0.5	0.5	0.5
LIF threshold	1.0	1.0	1.0
Output reset	None	None	None
Surrogate gradient	Fast sigmoid	Fast sigmoid	Fast sigmoid
<i>LSTM Architecture</i>			
Input size	96	96	96
Architecture	96-256-256-2	96-256-256-2	96-256-256-2
Layers	2	2	2
Dropout	0.2	0.2	0.2
<i>Kalman Filter</i>			
State dimensions	2 (velocity)	2 (velocity)	4 (pos+vel)
Observation dim	96	96	96
Process noise Q	0.1	0.1	0.1
Observation noise R	1.0	1.0	1.0
Initial covariance P	100.0	100.0	100.0
<i>Online SNN Learning</i>			
Fast learning rate	$1 \times 10^{-4}$	$1 \times 10^{-4}$	$1 \times 10^{-4}$
Slow learning rate	$1 \times 10^{-3}$	$1 \times 10^{-3}$	$1 \times 10^{-3}$
Meta learning rate	0.1	0.1	0.1
Window size K	10	10	10
$\tau_{\text{fast}}$	120ms	120ms	120ms
$\tau_{\text{slow}}$	700ms	700ms	700ms
Trace mixing $\alpha_{\text{mix}}$	0.5	0.8	0.5
Momentum $\mu$	0.9	0.9	0.9
Weight cap $c_{\ell}$	6.0	6.0	6.0
Weight decay	$1 \times 10^{-5}$	$1 \times 10^{-5}$	$1 \times 10^{-5}$
<i>Offline Training (LSTM &amp; BPTT-SNN)</i>			
Epochs	30	30	30
Batch size	64	64	64
Sequence length	50	5	50
Learning rate	$1 \times 10^{-3}$	$1 \times 10^{-3}$	$1 \times 10^{-3}$
Optimizer	Adam	Adam	Adam
Weight decay	$1 \times 10^{-5}$	$1 \times 10^{-5}$	$1 \times 10^{-5}$
Patience	10	5	10